THESIS FOR THE DEGREE OF DOCTOR OF PHILOSOPHY

Active sites and influence of reaction conditions on the selective catalytic reduction of NO_x over the silver-alumina catalyst

LINDA STRÖM

Department of Chemistry and Chemical Engineering
CHALMERS UNIVERSITY OF TECHNOLOGY
Göteborg, Sweden 2018

Active sites and influence of reaction conditions on the selective catalytic reduction of NO_x over the silver-alumina catalyst
LINDA STRÖM

ISBN: 978-91-7597-779-9

Doktorsavhandlingar vid Chalmers tekniska högskola
Ny serie nr. 4460
ISSN: 0346-718X

Department of Chemistry and Chemical Engineering
Chalmers University of Technology
SE-412 96 Göteborg
Sweden

Telephone: +46 (0)31-772 1000

Chalmers Reproservice
Göteborg, Sweden 2018

Active sites and influence of reaction conditions on the selective catalytic reduction of NO_x over the silver-alumina catalyst

LINDA STRÖM
Department of Chemistry and Chemical Engineering
Chalmers University of Technology

ABSTRACT

Hazardous nitrogen oxides (NO_x) are challenging to remove from fuel-efficient excess-oxygen operating engines. A promising solution is selective catalytic reduction (SCR) of NO_x, using hydrocarbons (HC-SCR) or ammonia (NH_3-SCR) as reducing agent. Highly efficient SCR of NO_x requires a fully understood system, which includes both the catalyst and the reducing agent. In this work, Ag/Al_2O_3 has been evaluated as an SCR catalyst with HC as well as NH_3 as reducing agents, in order to investigate the active sites and elucidate the influence of the nature of the reducing agent during lean NO_x reduction. In order to investigate the role of the active phase, Ag/Al_2O_3 was compared to an In/Al_2O_3 catalyst, containing the equivalent molar amount of active phase. In addition, the effect of an uneven distribution of the reducing agent is evaluated. Catalyst samples for which the active phase was synthesized in the water pools of a reversed microemulsion, using methanol as reducing agent for the metal complexes, was also prepared and evaluated. This work shows that the Ag/Al_2O_3 catalyst in general exhibits superior activity for NO_x reduction compared to In/Al_2O_3. However, since one of the hydrocarbon reductants was shown to reduce NO_x more efficiently over In/Al_2O_3, the exact nature of the reducing agent was shown to be of uttermost importance for the catalytic activity. In addition, the In/Al_2O_3 catalyst provides a higher concentration of acidic sites, compared to the Ag/Al_2O_3 catalyst, which was shown to inhibit the NH_3-SCR reaction over this catalyst. Furthermore, it was confirmed that the active phase can be tailored in a microemulsion synthesis containing a greener route than used in the past, resulting in catalytically active nanoparticles. Moreover, the position of the reductant injection spray in the exhaust pipe in front of the SCR catalyst was shown to significantly affect the NO_x reduction and unwanted slip of the reductant. The results presented in this thesis contribute to the overall understanding of the interplay between various active sites and reductants in SCR of NO_x, and may therefore help advance current technologies to improve the sustainability of future transports.

Keywords: Lean NO_x reduction, HC-SCR, NH_3-SCR, silver, indium, alumina, nanoalloys, microemulsion, UV-vis, DRIFTS, TEM, XRD, NH_3-TPD.

List of papers

I. **Hydrogen-assisted SCR of NO_x over alumina-supported silver and indium catalysts using C_2-hydrocarbons and oxygenates**
Linda Ström, Per-Anders Carlsson, Magnus Skoglundh & Hanna Härelind
Applied Catalysis B: Environmental **181** (2016) 403-412

II. **Surface species and metal oxidation state during H_2-assisted NH_3-SCR of NO_x over alumina-supported silver and indium**
Linda Ström, Per-Anders Carlsson, Magnus Skoglundh & Hanna Härelind
Catalysts **8** (2018) 38:1-14

III. **Quantification of urea-spray non-uniformity effects on the H_2-assisted NO reduction and NH_3 slip over an Ag/Al_2O_3 catalyst**
Linda Ström, Henrik Ström, Andreas Darnell, Per-Anders Carlsson, Magnus Skoglundh & Hanna Härelind
Energy Procedia **75** (2015) 2317-2322

IV. **Catalytically active Pd-Ag alloy nanoparticles synthesized in microemulsion template**
Linda Ström, Henrik Ström, Per-Anders Carlsson, Magnus Skoglundh & Hanna Härelind
Langmuir (2018) In press

Contribution report

I. I prepared the catalysts, performed all experimental work, interpreted the results together with my co-authors, wrote the first draft of the manuscript and was responsible for writing and submitting the manuscript.

II. I prepared the catalysts, performed all experimental work, interpreted the results together with my co-authors, wrote the first draft of the manuscript and was responsible for writing and submitting the manuscript.

III. I prepared the catalysts, performed all experimental work, interpreted the results together with my co-authors, partly wrote the first draft of the manuscript and was responsible for writing and submitting the manuscript.

IV. I prepared the catalysts, performed all experimental work, interpreted the results together with my co-authors, partly wrote the first draft of the manuscript and was responsible for writing and submitting the manuscript.

List of abbreviations

Ag/Al_2O_3	Silver-alumina
BET	Brunauer-Emmett-Teller, adsorption isotherm for determination of surface areas of solids
CEM	Controlled evaporator mixer
CFD	Computational fluid dynamics
C/N	Ratio between the number of carbon and nitrogen atoms
CO	Carbon monoxide
CO_2	Carbon dioxide
CPSI	Cells per square inch
DME	Dimethyl ether
DRIFTS	Diffuse reflectance infrared Fourier transform spectroscopy
HC	Hydrocarbons
In/Al_2O_3	Indium-alumina
N_2	Nitrogen
N_2O	Nitrous oxide
NH_3	Ammonia
NO_x	Nitrogen oxides (NO and NO_2)
NSR	NO_x storage and reduction
PGM	Platinum group metals
PM	Particulate matter
SCR	Selective catalytic reduction
SO_x	Sulfur oxides (SO_2 and SO_3)
TEM	Transmission electron microscopy
TPD	Temperature programmed desorption
TWC	Three-way catalyst
UV-vis	Ultraviolet and visible
XRD	X-ray diffraction

Contents

Chapter 1

Background

1.1 Historical development of exhaust aftertreatment

Global warming and air pollutants have received increased concern over the last decades, holding fossil fueled road transportation as one of the major responsible contributors. Among the emissions are carbon monoxide (CO), particulate matter (PM), sulfur oxides (SO_x), and nitrogen oxides (NO_x). The latter (almost exclusively NO) is, regardless of the chemical composition of the fuel, formed during combustion at high temperatures and is oxidized to NO_2 in the atmosphere. This gas is largely responsible for the brownish color of smog and plays a major role in formation of ground-level ozone. In the environment, this strongly oxidizing agent reacts in the air to form nitric acid as well as toxic organic compounds, which cause acidification and eutrophication. The effect of short-term exposure of NO_x to humans is still unclear, however, long term frequent exposure to concentrations higher than typically found in the ambient air, may cause increased incidence of acute respiratory illness [1]. In total, it is estimated that 500.000 people die each year as a result of the air pollutions from the transportation sector [2]. Furthermore, in Europe, close to 3 million ton NO_x was emitted just from road transportation in 2015 [3]. Figure 1.1 shows the total emissions of NO_x in the EU, divided by source.

Catalytic emission control has been applied to passenger cars in the US since 1975. This first version was able to oxidize unburned HC and CO. In 1981, a new catalytic system called the three-way catalyst (TWC) was developed, which operates under stoichiometric conditions and, except for oxidizing CO and HC, also reduces NO_x [2] (see Figure 1.2). Gasoline powered vehicles

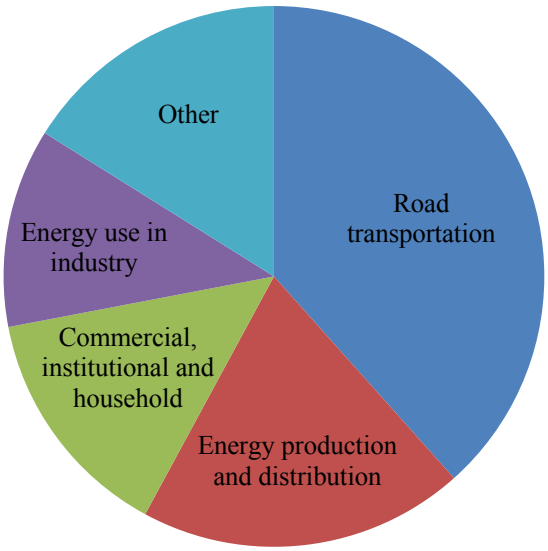

Figure 1.1: NO_x emissions divided by source sector in the EU in 2015.

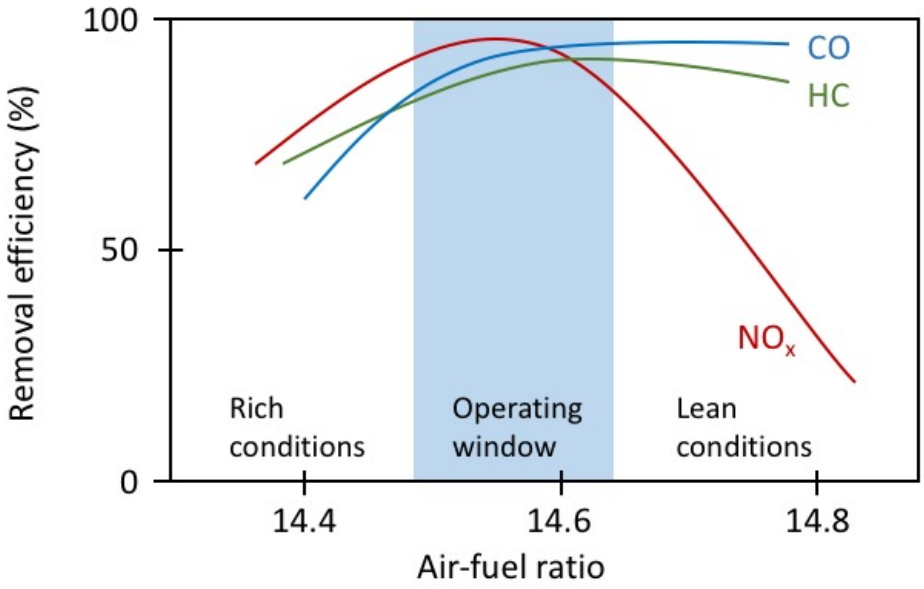

Figure 1.2: Illustration of the catalytic conversion of CO, unburned hydrocarbons and NO_x as a function of air-to-fuel ratio, over the TWC.

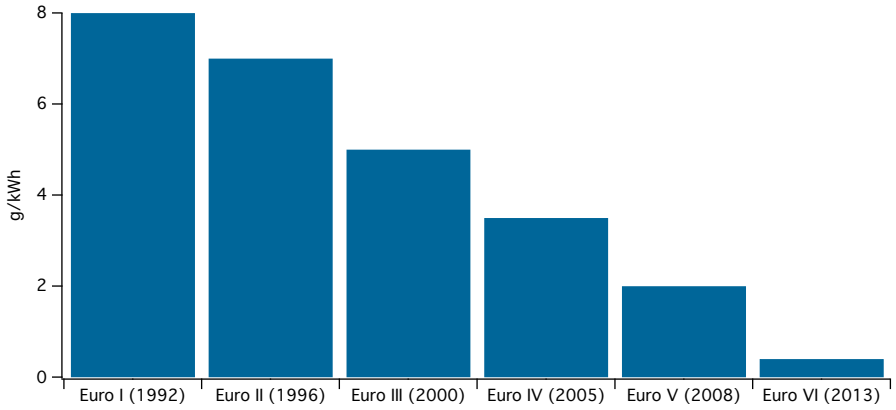

Figure 1.3: The historical development of Euro emission standards for NO_x emission for heavy-duty vehicles. Data for this chart is collected from Ref. [4].

operate under stoichiometric conditions and emissions provided by this type of engine can be effectively converted by the TWC. However, the climate change has gained increased concerns, motivating the development of more fuel-efficient engines, operating under lean conditions (excess oxygen) and in this way emitting less CO_2 per driven km, compared to the ordinary gasoline engine. However, lean conditions contradict the fundamentals of the TWC, hence another abatement technique is required for reducing NO_x. The legislation regarding NO_x emissions was first applied in Europe 1992 by the Euro I standard. Since then, the standard has been updated several times and Euro VI requires nowadays a NO_x emission of no more than 0.4 g/kWh [4]. The development of Euro-standards of NO_x emissions is shown in Figure 1.3.

Techniques for lean NO_x reduction at present involve selective catalytic reduction with ammonia (NH_3-SCR) and NO_x storage and reduction, which are already implemented techniques. Also selective catalytic reduction using hydrocarbons (HC-SCR) is an interesting solution. However, even though HC-SCR would represent an elegant technological solution to the NO_x reduction challenge, the technique is not yet mature for commercialization. Owing to the complexity of the technique, a more in-depth knowledge can also be expected to produce added value in terms of a more comprehensive understanding of the fundamental heterogeneous catalysis involved. A promising catalyst for HC-SCR is silver-alumina (Ag/Al_2O_3) [5-9], which shows high stability in hydrothermal conditions [10]. All of the mentioned techniques are further introduced in the next chapter.

1.2 Objectives

The aim of this work is to develop the understanding of the selective catalytic reduction of NO_x over the silver-alumina catalyst. In particular, the impact of the nature of the reducing agent on the catalytic activity as well as the effect of the surrounding gas phase environment on the active sites are studied. Furthermore, the effect of a non-uniform reductant distribution on the NO_x reduction activity and reductant slip is discussed.

In order to evaluate the impact of the active phase on the catalytic activity, a silver-alumina catalyst is compared to alumina-supported indium, holding the equivalent molar amount of metal. In addition, catalytically active Ag-Pd alloys synthesized in a microemulsion-template elucidate the impact of the surface structure.

Chapter 2

Catalysis for lean NO_x reduction

2.1 NO_x reduction during lean conditions

Development of lean NO_x reduction catalysts for usage in vehicles involves several challenges. For example, the engine operates under transient loading, which results in variations in temperature and flow rate of the exhaust stream over time. Hence, a successful catalyst should be able to operate properly over a wide temperature range and exhaust flow rate. During lean operation in energy efficient engines, such as the diesel engine, the exhaust temperature of a heavy-duty vehicle is around 100-200 ℃ during idling and about 500 ℃ during maximum load [11]. The lean NO_x reduction catalyst must therefore be able to operate effectively at these low temperatures. Furthermore, the catalyst is subjected to small amounts of electronegative elements such as sulfur and phosphorus, which tend to adsorb strongly to the surface and poisoning the catalyst by physical or electronic blockage of active sites [12]. Another degradation mechanism is sintering of the active phase, which leads to loss in surface area and an increase in the average surface coordination. Formation of volatile compounds, containing the active phase, also contributes to catalyst depletion, as well as fouling of pores. In addition to these demands on a successful lean NO_x reduction catalyst to provide high activity at low temperature and avoiding degradation, space limitations onboard a vehicle needs to be considered.

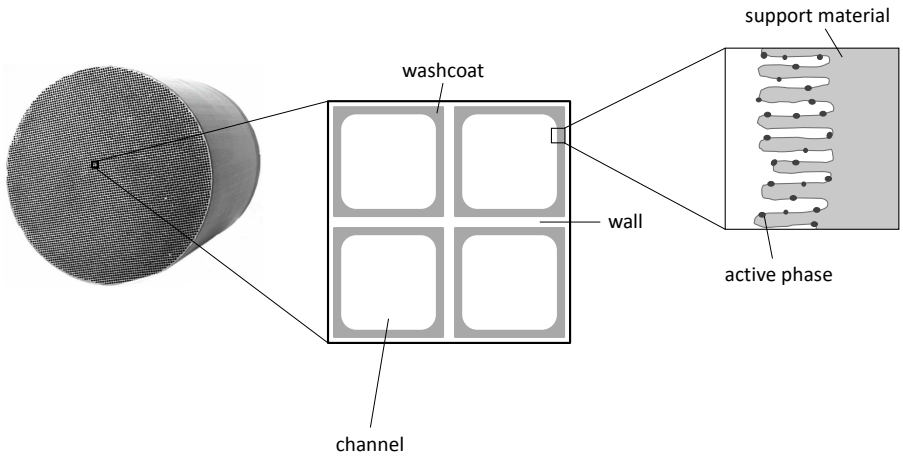

Figure 2.1: A schematic illustration of a monolithic reactor with the entrance of four individual channels and the catalytically active washcoat enlarged.

2.2 Methods for conversion of NO_x

Monolithic reactors, consisting of thousands of channels, are standard for vehicle emission control today. These monolithic substrates are typically made of a ceramic material such as cordierite, but can also be metallic. The catalyst, which consists of an active phase and a highly porous support material, providing a large surface area, is coated onto the substrate. Figure 2.1 shows a typical monolithic catalyst. In this section, some of the techniques for lean NO_x reduction is presented.

2.2.1 NO_x storage and reduction

An implemented technique for lean NO_x reduction is NO_x storage and reduction (NSR), where Pt and BaO supported on Al_2O_3 is the most commonly used catalytic material. In this approach, NO is first oxidized to NO_2 over Pt and subsequently adsorbed as stable nitrite or nitrate species on the storage material BaO during a lean phase, which lasts for 1-2 minutes. During a subsequent rich (oxygen deficiency) period of 3-5 seconds, the trapped NO_x is released and reduced to N_2 by unburned fuel and CO over Pt [13-15]. Drawbacks of this technique include the complexity of the engine system and fuel penalty during the rich periods [16]. Also, the formation of stable sulfates with the NO_x-storage material and the oxide support makes the

NSR-catalyst degrade over time, and in requirement of regeneration, which is usually performed under high temperatures (>600 ℃) and during the rich part of the cycle [17].

2.2.2 Hydrocarbon-SCR

Another feasible solution for lean NO_x reduction is selective catalytic reduction using hydrocarbons (HC-SCR) [7, 18-23]. In this approach, the hydrocarbon-based fuel is injected into the exhaust system upstream the SCR catalyst and used as reducing agent for NO_x over the catalyst. An advantage of using the fuel as the reductant is that there is no need for an additional tank for reductant storage onboard the vehicle. However, some of the challenges regarding this technique, are to receive high conversion of NO_x with high selectivity to N_2 despite high oxygen concentration, low temperature, transient loadings and exposure to sulfur and water.

The exact reaction scheme of lean NO_x reduction with hydrocarbons is still under debate. However, some general differences have been detected over different types of catalysts, based on noble metals, oxides or zeolites. The TWC is based on various combinations of noble metals such as Pt, Pd and Rh as the active phase and converts HC, CO and NO_x effectively under stoichiometric conditions at 400-800 ℃. Since this catalyst proved to be completely ineffective for NO_x reduction during large excess of oxygen, the platinum group metals (PGMs) were first assumed to be incapable of reducing NO_x in lean conditions. However, although PGM-based catalysts are ineffective at moderate or high temperatures, they have shown to be active for NO_x reduction at low temperatures (typically below 300 ℃) [18]. Reaction mechanisms proposed for lean NO_x reduction by short-chained alkene-type hydrocarbons over Pt are *i*) the intermediacy of cyanide or isocyanate surface species, *ii*) the intermediacy of organo-nitro species and *iii*) decomposition of NO followed by oxygen removal by the HC [18].

NO adsorbs as strongly bound nitrites and nitrates in excess oxygen (but adsorbs only weakly in absence of oxygen) on most catalyst surfaces [24]. Over oxide based catalysts, the first step in the reaction mechanism is proposed to be the surface adsorption of NO_x. Adsorbed oxidized hydrocarbon species, such as acetate [22, 25], are formed during SCR with various hydrocarbons or oxygenates over alumina-based catalysts, and are believed to react with the adsorbed NO_x species, yielding organo-nitrogen species, which appears to be the rate-determining step [18]. Via these species, reduced nitrogen species, such as –NCO (isocyanate) and NH_3 can be formed. It has been proposed

that the nitrogen coupling to form N_2 could occur by a reaction between these reduced species and NO (g) or adsorbed NO_x [18, 26].

2.2.3 Ammonia-SCR

NH_3-SCR is an implemented automotive technology for NO_x removal from diesel exhaust [27, 28]. Traditional active metal oxides used in NH_3-SCR are V_2O_5, WO_3 and MoO_3 [15], where the vanadium-based catalyst is the most active for lean NO_x removal. However, usage of this highly toxic catalyst pose some serious problems involving high vapor pressure of the oxide leading to toxic emissions [29], which calls for new types of catalytic materials.

To avoid storage and handling issues of ammonia, the reductant is injected to the exhaust system as a urea-water solution which decomposes to ammonia over the catalyst. Alumina has been shown to be especially suitable for this decomposition [29]. The reducing agent could also be produced on-board by so-called 'passive SCR' [30, 31]. However, there are some disadvantages regarding NH_3-SCR, such as distribution of the urea solution and the possibility that unreacted ammonia is emitted (so called ammonia slip) [32].

2.3 Alumina-supported catalysts

Alumina-supported catalysts have received much attention thanks to their high stability under hydrothermal conditions. The alumina phase most widely used for this purpose is the porous and amorphous γ-Al_2O_3, which provides a large surface area (100-300 m^2/g). This support material is prepared by calcination of Boehmite (AlO(OH)) or Bayerite/Gibbsite ($Al(OH)_3$) at 500-850 ℃.

2.3.1 The Ag/Al_2O_3 catalyst

Miyadera was the first reporting on alumina-supported silver (Ag/Al_2O_3) catalysts in 1993 [33]. Ever since, a major interest has been directed towards this catalyst, which exhibits SCR activity both with ammonia [34-38] and hydrocarbons [21, 33, 39-41]. The optimal silver loading has been frequently studied and it has been found to be around 2 wt.% for impregnated catalysts [8, 22, 26, 42, 43]. The reason for this has been suggested to involve the optimal silver density, which should be close to 0.7 Ag/nm^2 [44].

The species active for SCR of NO_x has been assigned to Ag^+-ions [22, 45, 46] and small clusters of ionic silver ($Ag_n{}^{\delta+}$, $n \leq 8$) [35, 46], or a combination

of these. Metallic silver particles have been assigned to be active for total oxidation of the reductant by molecular oxygen [26]. Moreover, it has also been suggested that active sites of Ag/Al_2O_3 varies as a function of the reductant type and reaction temperature [23]. Over Ag/Al_2O_3, the following reactions are proposed to be involved: *i*) oxidation of NO to NO_2 followed by the formation of surface nitrites and nitrates, *ii*) adsorption and partial oxidation of hydrocarbons, and *iii*) surface reactions between the adsorbed nitrogen species and the partially oxidized hydrocarbons [14].

The 'hydrogen effect'

The addition of small amounts of hydrogen to the gas feed increases significantly the NO_x reduction activity over the Ag/Al_2O_3 catalyst. This phenomenon was first discovered by Satokawa [47], and has later been widely studied [7, 36, 44, 48]. The effect is rapidly reversible, so addition/removal of hydrogen from the feed increases/decreases the SCR activity instantly. Such cycles can be repeated without loss in catalytic performance [7, 46]. Moreover, the mechanism(s) behind this promotion has been widely debated. Suggestions involve reduction of adsorbed nitrogen species [48-51], enhanced activation of the hydrocarbon in HC-SCR [32, 43, 48-50], modification of the Ag-species [35, 46, 51, 52], as well as direct effects on the reaction mechanism [51, 54]. During NH_3-SCR, Ag/Al_2O_3 lacks in activity without the presence of hydrogen in the feed while NO_x is completely converted at relatively low temperatures when hydrogen is present [34]. Also In/Al_2O_3 exhibits the hydrogen effect during NH_3-SCR, however, to a lower extent compared to Ag/Al_2O_3 [55].

Chapter 3

Scientific methods and research approach

3.1 Catalyst preparation

In paper I, II and III, the catalytic samples were prepared by incipient wetness impregnation and coated onto monolithic substrates for evaluation. In paper IV, the active phases of the catalysts were synthesized in the water pools of reversed (w/o) microemulsions. Here follows a description of the specific methods.

3.1.1 Incipient wetness impregnation

The support material γ-Al_2O_3 (PURALOX® SBa 200, Sasol) was impregnated by the incipient wetness technique, where the added volume of solution containing the active metal complex is equal to or less than the pore volume of the support. This impregnation technique is also known as pore-volume or dry impregnation and depends more on retaining the active phase within the pores during drying rather than interactions. An advantage of this method is that the mass of the added components can easily be controlled [56].

The pore volume of the alumina was determined by slow addition of water that migrate into the pores. When the support is saturated the powder receives a creamy consistence and the water volume consumed corresponds to the pore volume. The active phase precursors used were silver nitrate ($\geq$ 99.0% Sigma-Aldrich) for the Ag/Al_2O_3 sample and indium nitrate hydrate (99.99% Sigma Aldrich) for the In/Al_2O_3 sample. The Ag loading was 2 wt.% and the In loading corresponded to the equivalent molar amount, giving an In loading of 2.1 wt.%. After adding the precursors, the samples were frozen

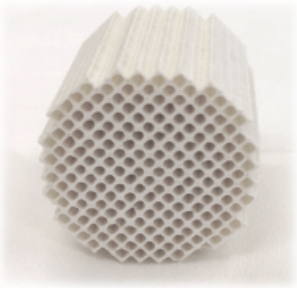

Figure 3.1: A monolith coated with Ag/Al_2O_3.

by liquid nitrogen, then freeze-dried and finally calcined in air at 600 ℃ for four hours.

Monolith coating

The catalytic samples prepared by incipient wetness impregnation were coated onto substrates before the evaluation of catalytic activity. Monoliths with 188 channels (400 CPSI, Ø = 20 mm, L = 20 mm) were cut from a commercial cordierite honeycomb structure (Corning) and calcined in air at 600 ℃ for one hour. Washcoat slurries were prepared, containing binder agent (DISPERAL® P2, Sasol) and one of the powder catalysts (ratio 1:4) in 1:1-ratio ethanol-water solutions. Monoliths were dipped into the slurries, gently shaken for removal of excess slurry, dried in a 90 ℃ hot air stream and subsequently calcined at 500 ℃ for 3 minutes. The coating procedure was repeated until the washcoat mass corresponded to 20% of the coated monolith mass. Finally, the monoliths were calcined in air at 600 ℃ for one hour. A coated monolith sample is shown in Figure 3.1.

3.1.2 Microemulsions as nanosized reactors

Macroscopically, microemulsions are homogenous mixtures of oil, water and surfactant. Despite the name, microemulsions and ordinary emulsions are fundamentally different and the latter should not be regarded as microscopic emulsions. Ordinary emulsions are unstable, static systems with droplet sizes of 1-10 μm, while microemulsions are highly dynamic, stable systems with aggregates of 1-10 nm [58].

In paper IV, catalytically active bimetallic nanoparticles were synthesized in the water pools of reversed (w/o) microemulsions, holding 75 wt.% oil, 20 wt.% surfactant and 5 wt.% water. The surfactant dioctyl sulfosuccinate

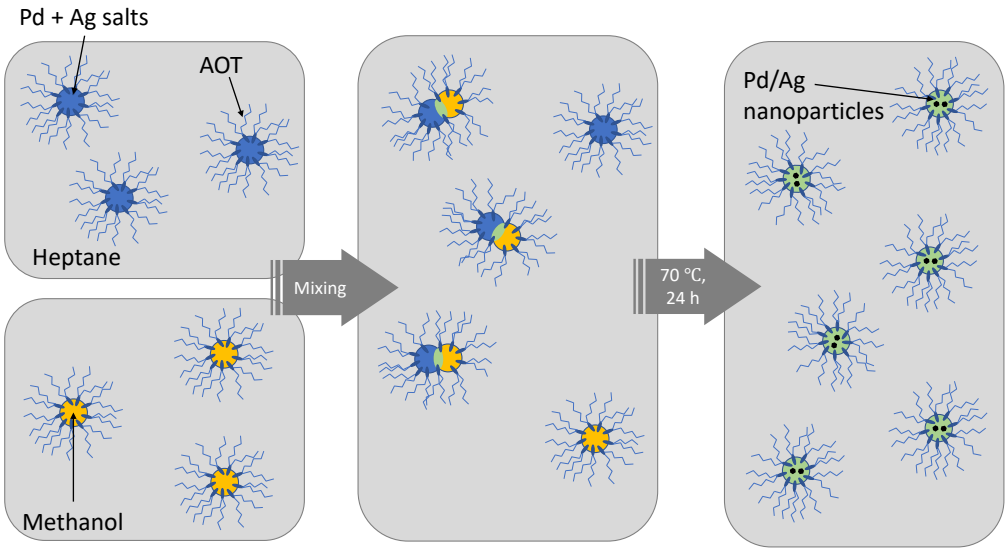

Figure 3.2: Illustration of the nanoparticle synthesis procedure. The metal salt-containing microemulsion is mixed with the microemulsion containing methanol. Subsequently, the mixture is allowed to react at 70 °C for 24 h.

sodium salt (98% Aldrich Chemistry), hereafter denoted AOT, was dissolved in heptane (Reag. Ph. Eur. Riedel-de Haën) in a wt. ratio of 1:4. Subsequently, aqueous solutions of silver nitrate (>99% Sigma-Aldrich) and/or palladium(II) nitrate (15% Alfa Aesar), both holding 2 wt.% metal, were added. Samples containing palladium only, silver only, 20/80, 40/60 and 50/50 wt.% of each metal precursor were prepared. During preparation of samples containing both elements, the palladium precursor was added prior to the silver precursor.

In order to reduce the metallic precursors into metallic nanoparticles, another microemulsion was added to the first, consisting of a water phase with 50 wt.% methanol. Subsequently, the microemulsion mixture is allowed to react at 70 °C for 24 h. The synthesis procedure is illustrated in Figure 3.2.

3.2 Characterization techniques

3.2.1 N_2 sorption

The specific surface area of a solid material can be determined according to the method published in 1938 by Brunauer, Emmett and Teller [59] (the BET-method). The technique is based on physical adsorption of an inert

gas (most often molecular nitrogen) on the surface of the solid material. Generally, the method provides reliable values of the surface area, unless the sample involves micropores, where the size of the pores in the adsorbent and the size of the adsorbate molecule are similar [59]. The method assumes that *i*) the heat of adsorption of the first monolayer is constant, *ii*) the lateral interaction of the adsorbate is negligible, *iii*) the adsorbed molecules can act as new adsorption surface and the process can repeat itself and *iv*) the heat of adsorption of all monolayers but the first is equal to the heat of condensation [60]. In practice, the sample is first heated up under vacuum to remove moisture and subsequently cooled down to 77 K by liquid nitrogen. At this temperature N_2 is dosed in small volumes and the pressure is allowed to stabilize. The physisorbed volume of N_2 can now be calculated using the ideal gas law. Knowing the area of one adsorbed N_2-molecule, the specific surface area of a sample can be derived from the following formula:

$$\frac{P}{V(P_0 - P)} = \frac{1}{V_\mathrm{m}C} + \frac{C-1}{V_\mathrm{m}C}\frac{P}{P_0} \tag{3.1}$$

where P is the equilibrated partial pressure, V is the volume of absorbed gas, P_0 is the saturation pressure and V_m is the inert gas monolayer volume. At low pressure, the relationship between $P/V(P_0 - P)$ and P/P_0 is linear, hence it follows that $1/V_\mathrm{m}C$ is where the straight line intercepts the y-axis and $(C-1)/(V_\mathrm{m}C)$ is the slope of the line.

In Paper I, II and III, N_2 sorption according to the BET-method was used to determine the specific surface area of the powder catalyst samples using a Micrometrics TriStar® 3000 instrument.

3.2.2 X-ray diffraction

The non-destructive technique X-ray diffraction (XRD) can be used to examine the crystal phase of a sample. When irradiated by X-rays with the wavelength λ, electron clouds of the crystal-structured atoms scatter the X-rays, which are measured by a detector. The distance between the lattice planes, d, can then be calculated by Bragg's law:

$$n\lambda = 2d\sin\Theta \tag{3.2}$$

Where n is any integer and Θ the incident angle.

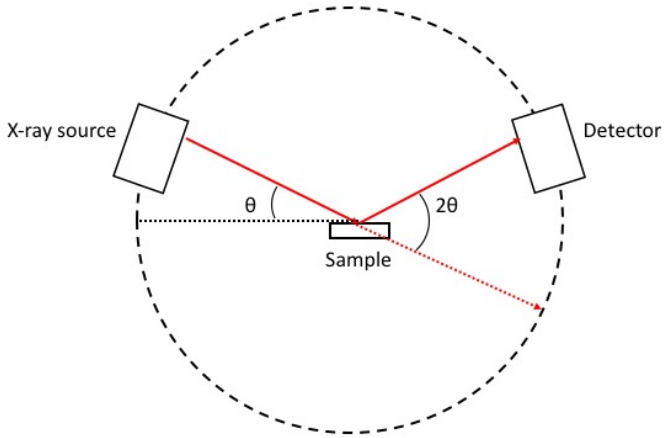

Figure 3.3: Illustration of an X-ray diffraction experiment.

A Siemens D5000 X-ray diffractometer was used for evaluation of crystalline phases in Paper I and a Bruker D8 Advance X-ray diffractometer was used in Paper IV. The incident beam angle was varied between 5-90° with a step size and time of 0.02° and 1 s, respectively. An illustration of the technique is showed in Figure 3.3.

3.2.3 Temperature programmed desorption of NH_3

The density and strength of the acidic sites of a catalytic sample can be characterized by temperature programmed desorption (TPD) of NH_3. In paper I-III, the flow reactor described in section 3.3 was used for this experiment. Prior to NH_3 adsorption, the sample is pretreated to remove possible carbonaceous matter. By saturating the catalytic sites by this strong base at low temperature (around 100 ℃) and then slowly increase the temperature, the amount of NH_3 able to chemisorb to the sites at low temperature is desorbed and can be measured. Weakly adsorbed NH_3 is released first and more strongly bound at somewhat higher temperatures, which gives the possibility to distinguish between different kinds of acidic sites.

3.2.4 UV-visible diffuse reflectance spectroscopy

Electronic *d*-*d* transitions are observable in the ultraviolet and visible light region (200-2000 nm) when degenerated *d* orbitals are split by placing a transition metal ion in a crystal field. Furthermore, the number of *d*-electrons,

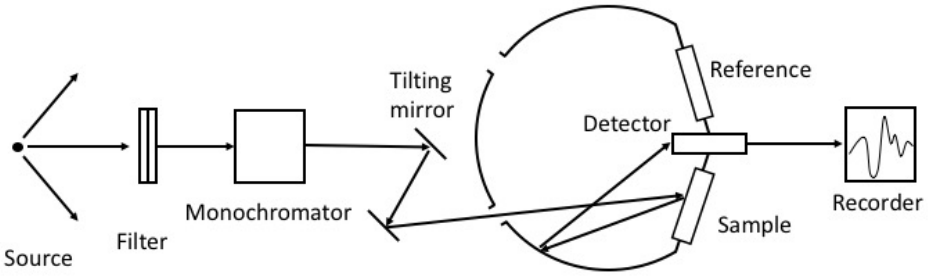

Figure 3.4: A schematic diagram of a UV-vis spectrometer operating in the diffuse reflectance mode. Adapted from Ref. [62].

the effective charge on the ion and the distribution and charge of the surrounding anions are circumstances that affect the spread of the energy levels [62]. Consequently, the technique can be used for characterization of the types of species present in a solid sample. A typical beam path is visualized in Figure 3.4.

In this study, UV-vis was used to characterize the oxidation states of the samples studied in Paper I and II, where spectra have been deconvoluted into Gaussian peaks. Spectra in the range 200-1500 nm were recorded using a Varian Cary 5000 UV-vis-NIR spectrophotometer equipped with an external DRA-2500 unit. The reflectance spectra were recorded and the spectrum of the Al_2O_3 support was subtracted as part of the background. To investigate the influence of reaction conditions on the type of surface species, both fresh catalysts and samples exposed to various gas-phase pretreatments, using the flow reactor described below (Section 3.3), were analyzed.

3.2.5 Transmission electron microscopy

Transmission Electron Microscopy (TEM) provides a two-dimensional projection showing details in resolution down to 1 nm [63]. A primary electron beam of energy between 100 and 300 keV hits the sample, which is coated onto a grid, resulting in a fraction (depending on sample thickness) of electrons that transmit the sample without any significant energy loss, projecting a two-dimensional image of the sample [64]. In addition, Energy Dispersive X-Ray Spectroscopy (EDX) can be combined with a microscope, providing spatial mapping of the atomic composition within a sample [63]. Figure 3.5 shows an illustration of a microscope in intersection together with the electron scattering.

In paper IV, TEM images were received using a FEI Tecnai T20 electron

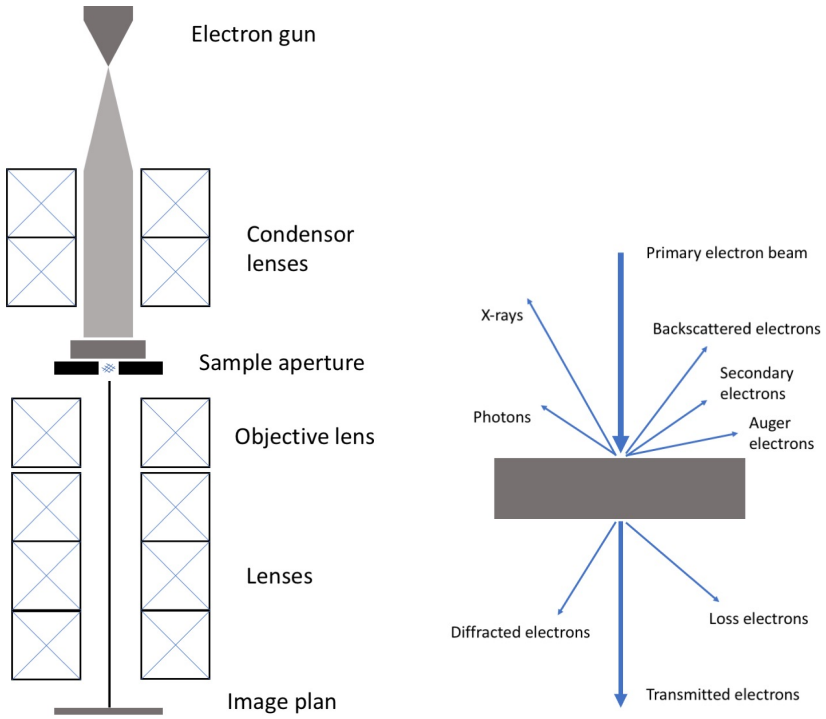

Figure 3.5: a) A transmission electron microscope in intersection and b) the scattering of electrons. Both figures are adapted from reference [64].

microscope operating at 200 kV. The distribution of the elements within a nanoparticle was investigated using scanning TEM coupled with energy-dispersive X-ray spectroscopy, using a FEI Titan 80-300 microscope operating at 300 kV. This microscope was also used for analysis of the samples supported on γ-alumina in Scanning TEM mode using a high-angle annular dark-field (HAADF) detector, where the STEM images display a combined mass-thickness contrast.

3.2.6 *In situ* Fourier transform infra-red spectroscopy

One of the most widely used tools for surface science is Diffuse Reflectance Infrared Fourier Transform Spectroscopy (DRIFTS) [64]. During reaction conditions, in *in situ* mode, it can characterize adsorbed surface species, such as reactants and intermediate species, as well as gas phase products.

Molecules possess discreet vibrational and rotational energy levels. The technique relies on the transition between vibrational energy levels by the absorption of photons. A photon can only be absorbed by a molecule if its dipole

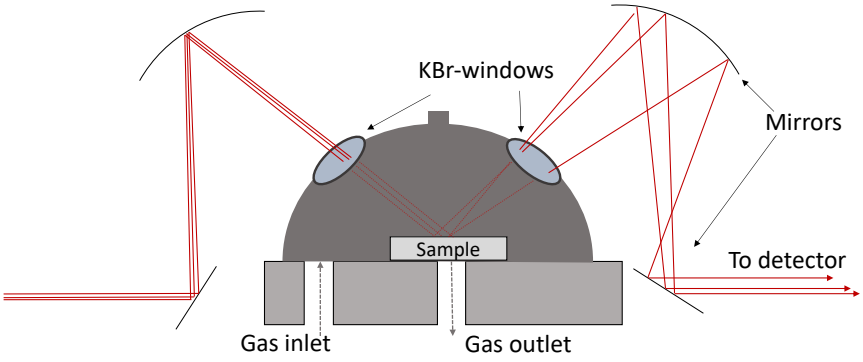

Figure 3.6: Illustration of the beam path and gas flow of the DRIFTS reaction cell.

moment changes during the vibration. The technique is therefore limited to detection of molecules that follow this rule, [64].

In the gas phase, the molecules have rotational freedom and the vibrational transition can not be observed, but two side bands appear instead. Upon adsorption of the molecule, its ability to rotate is lost and only the vibrational transition is observed, however, often at another frequency [64].

In paper II and IV, *in situ* DRIFT spectra were recorded using a Bruker Vertex 70 spectrometer equipped with a high-temperature reaction cell (Harrick Scientific) with KBr windows. Figure 3.6 shows an illustration of the instrument setup.

3.3 Evaluation of catalytic performance

The catalytic activity for lean NO_x reduction was examined during extinction ramps (500 to 100 ℃ by 10 ℃/min), using a flow reactor illustrated in Figure 3.7. The reactor chamber consists of an insulated horizontal quartz tube (L = 80 cm, $\varnothing_i$ = 22 mm) heated by a metal coil. The catalyst temperature is measured inside the sample and the reactor temperature is controlled 15 mm before the catalyst sample by K-type thermocouples. Uncoated monoliths placed before and after the coated monolith shield the thermocouple from heat radiation emitted by the heating coil as well as reduce axial radiation

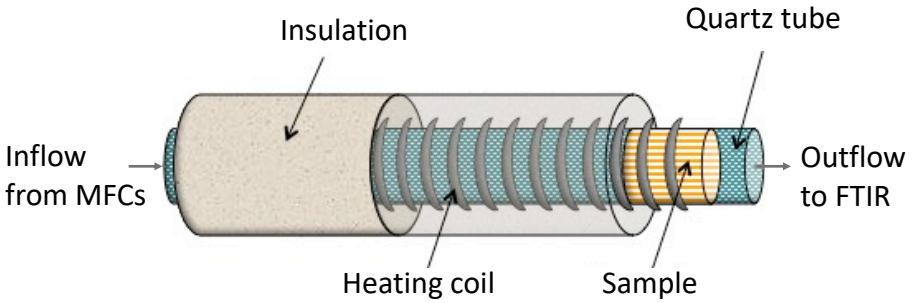

Figure 3.7: Illustration of the flow reactor used in the NO_x reduction experiments, UV-vis pretreatments and for the NH_3-TPD.

heat losses from the coated monolith sample [65]. The inlet feed gases are introduced and regulated by mass-flow controllers (Bronkhorst Hi-Tech) and the outlet gas flow is analyzed by a gas-phase FTIR spectrometer (MKS 2030). Fluent hydrocarbons/oxygenates and water are introduced to the reactor via a controlled evaporator mixer system (CEM, Bronkhorst Low ΔP Hi-Tech), carried by Ar.

The total gas flow was set to 3500 ml/min in all experiments, which corresponds to a space velocity (GHSV) of 33,400 h^{-1}. Prior to each measurement, the sample was pretreated in O_2 (10%, Ar balance) at 500 ℃ for 30 min. In the HC-SCR study, the gas feed composition was 500 ppm NO, 1500 ppm C_2-hydrocarbon (C/N ratio of 6, in line with previous experience [35, 37]), 10% O_2 and 5% H_2O, in the presence or absence of 1000 ppm H_2. The C_2-hydrocarbons and oxygenates used are ethane, ethene, ethanol, acetic acid and DME, respectively, with the structures shown in Figure 3.8 (Paper I). In the NH_3-SCR study (paper II and III), the gas composition was 500 ppm NO, 500 ppm NH_3, 1000 ppm H_2, 10% O_2 and 5% H_2O.The reduction of NO_x and conversion of reducing agents were obtained from the ratios of the differences between the inlet and outlet concentrations to the corresponding inlet concentration.

In addition to lean NO_x reduction and NH_3-TPD experiments, this reactor setup was also used for the UV-vis pretreatments of Paper I and II, using a flow rate of 100 ml/min.

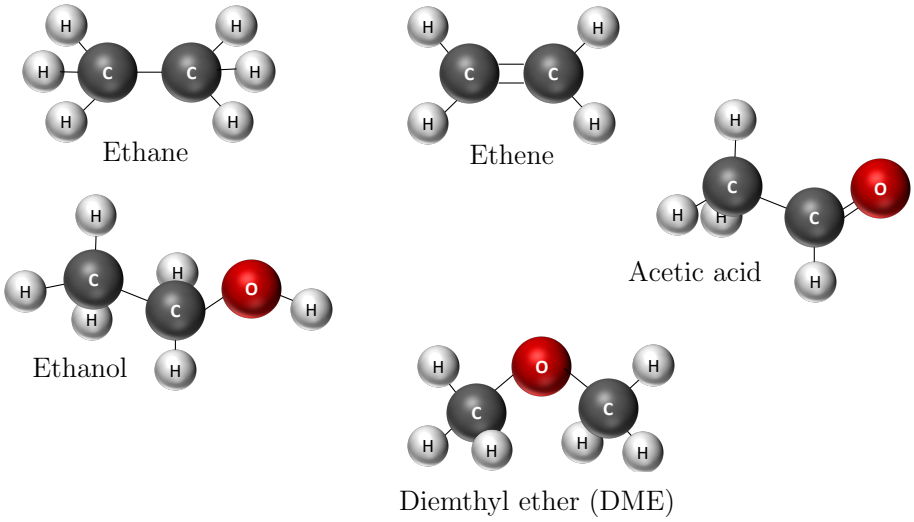

Figure 3.8: Structures of the hydrocarbons and oxygenates used as reductants.

Chapter 4

Results and discussion

In this chapter, the results of this work are presented. First, the influence of the specific reducing agent on the lean NO_x reduction activity is evaluated. The reductants compared are various C_2-hydrocarbons (paper I) as well as NH_3 (paper II), with and without H_2-assistance. In addition, the effect of a non-uniform dosage of the reducing agent is discussed (paper III). Thereafter, focus is paid on the active sites and how they are affected by the surrounding gas composition (paper I-II). Furthermore, the possibility to alter the catalytic activity by tuning the active sites is investigated (paper IV). Here, Ag/Pd alloy nanoparticles, which can possess other properties than the respective element alone, are synthesized in a reversed microemulsion template.

4.1 Influence of the reducing agent on lean NO_x reduction

The influence of the nature of the reducing agent for lean NO_x reduction over Ag/Al_2O_3 was investigated using a variety of C_2-based hydrocarbons as well as ammonia. In addition, the influence of adding a small amount of hydrogen to the reaction was investigated. The reaction scheme for SCR of NO_x over silver-alumina catalysts comprises a number of interconnected reactions such as oxidation of NO to NO_2 with the subsequent formation of surface nitrites and nitrates, and activation of the reducing agent before reduction of NO_x [14]. The activation of the reducing agent has been proposed to be the rate-determining step [35]. The final reaction products are ideally N_2, CO_2 and H_2O.

The promoting effect of H_2 on NO_x reduction has previously been believed

to be limited to silver-based catalysts [7]. However, recently it was discovered that also alumina-supported indium exhibits the H_2-effect. Therefore, the inherent properties and catalytic activity of the Ag/Al_2O_3 catalyst is compared to an In/Al_2O_3 sample, prepared in the same way and holding the equivalent molar amount of active phase. During the SCR experiments presented in Paper I-II, the inlet gas feed was carried by argon and composed of 500 ppm NO, 10% O_2, 1500 ppm HC (ethane, ethene, ethanol, acetic acid or DME, resulting in a C/N ratio of 6) or 500 ppm NH_3 as reducing agent. The experiments were carried out with and without the addition of 1000 ppm H_2. Below, the results of the NO_x reduction experiments are presented and discussed.

4.1.1 Catalytic activity

The ability of the Ag/Al_2O_3 and In/Al_2O_3 catalysts to reduce NO_x using the five hydrocarbon-based reductants and ammonia as reducing agents are shown in Figure 4.1. It can be clearly distinguished that the activity for NO_x reduction differs significantly, both among the reductants and between the catalysts. Over Ag/Al_2O_3 the highest NO_x conversion is achieved using ethane (90% conversion at 500 ℃) and ethene (88% at 500 ℃), during H_2-assistance. With these reductants, the enhancing effect of hydrogen addition on the catalytic activity is well pronounced over the Ag/Al_2O_3 catalyst, which exhibits an increase in the overall NO_x reduction, an increase in the low-temperature activity and a broadening of the active temperature window. Moreover, over In/Al_2O_3, the addition of hydrogen clearly enhances the reduction of NO_x with ethane, from 5% without the presence of H_2, to 17% at 500 ℃ with hydrogen in the gas feed. The overall highest activity received over the In/Al_2O_3 catalyst is achieved with ethene as reductant (50% NO_x reduction at 500 ℃).

Similar to hydrogen-assisted ethane- and ethene-SCR, also SCR with acetic acid results in an increased low-temperature activity and a broadened active temperature window of NO_x conversion in the presence of hydrogen over the Ag/Al_2O_3 catalyst. In general, NO_x is reduced less efficiently over the In/Al_2O_3 catalyst compared to the Ag/Al_2O_3 catalyst. However, with DME as reducing agent, no reduction of NO_x can be observed over the Ag/Al_2O_3 catalyst, while the NO_x conversion reaches 45% at 365 ℃ over the In/Al_2O_3 catalyst.

The Ag/Al_2O_3 catalyst exhibits a broad active temperature window for NO_x reduction with ethanol, starting at 260 ℃ (250 ℃ with hydrogen-assisted

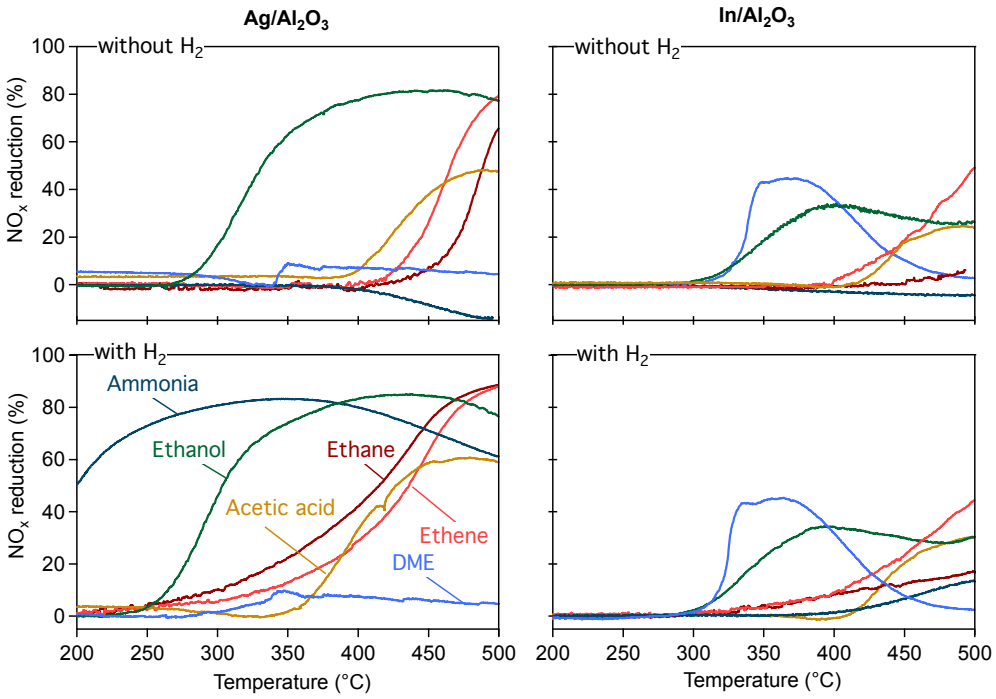

Figure 4.1: Lean NO_x reduction over alumina-supported silver (to the left) and indium (to the right) using a variety of C_2-based hydrocarbons and ammonia, with H_2-assistance in the bottom graphs.

ethanol) and peaking at 82% NO_x conversion at 440 °C. The selectivity towards N_2 is high, in accordance to literature [34, 66]. The highest low-temperature activity is achieved with NH_3 over Ag/Al_2O_3 when H_2 is added, reaching 80% conversion at 350 °C with a light off temperature at 200 °C. However, using the same reductant over the same catalyst but without the addition of H_2 results in no activity at all, or even negative values, which is likely due to the oxidation of NH_3 to NO [34]. The In/Al_2O_3 catalyst is unable to reduce NO_x with NH_3 solely. However, with the addition of H_2, the NO_x conversion clearly increases, however, to a significantly lower extent compared to Ag/Al_2O_3. The results presented in this section shows that the activity for NO_x reduction varies considerably, both when comparing the catalysts and when comparing the reducing agents.

4.1.2 Reaction products

The conversion of the hydrocarbon-based reducing agents, together with the formation of CO and CO_2 during the NO_x reduction experiments are shown

Table 4.1: The highest byproduct concentrations (in ppm) formed by the oxygenated reductants in the SCR experiments.

	Acetic acid (+H_2)		DME (+H_2)		Ethanol (+H_2)	
	Ag/Al_2O_3	In/Al_2O_3	Ag/Al_2O_3	In/Al_2O_3	Ag/Al_2O_3	In/Al_2O_3
Ethanol	32 (25)	29 (56)	6 (7)	6 (8)	-	-
Methanol	≤5 (≤5)	≤5 (≤5)	88 (84)	974 (991)	23 (19)	35 (33)
Acetaldehyde	45 (45)	47 (58)	34 (31)	29 (28)	406 (393)	367 (352)
Formaldehyde	57 (93)	87 (99)	27 (34)	171 (179)	34 (37)	25 (23)
Ethene	5 (≤5)	18 (26)	≤5 (≤5)	≤5 (≤5)	61 (54)	355 (382)
Methane	13 (11)	16 (18)	≤5 (≤5)	≤5 (≤5)	6 (6)	7 (5)
N_2O	≤5 (≤5)	≤5 (≤5)	≤5 (≤5)	15 (14)	9 (14)	6 (6)
Ammonia	28 (24)	24 (27)	≤5 (≤5)	≤5 (≤5)	114 (121)	22 (12)

in Figure 4.2 (Ag/Al_2O_3) and 4.3 (In/Al_2O_3). A trend can be distinguished where conversion of the saturated hydrocarbon (ethane) is low, the conversion of the unsaturated hydrocarbon (ethene) is higher and the oxygenated hydrocarbons (ethanol, DME and acetic acid) are almost completely converted. Ethanol is fully converted around 350 ℃ over both catalysts, as shown in Figure 4.2-4.3. DME is almost fully converted just above 300 ℃ over both catalysts. However, Ag/Al_2O_3 combust DME more completely, compared to In/Al_2O_3, as shown by the CO_2 to CO-ratio in these figures. In addition, various N- and C-containing species formed during the SCR experiments were detected in the outlet gas flow.

The main byproducts formed over the two catalytic samples using the oxygenated hydrocarbons are summarized in Table 4.1. Significant are the formation of acetaldehyde over both catalysts and NH_3 over Ag/Al_2O_3 from ethanol-SCR. This reducing agent also converts to a significant amount of ethene over In/Al_2O_3. Also methanol and formaldehyde formation over In/Al_2O_3 during DME-SCR should be mentioned.

NH_3 is highly active for SCR of NO_x over Ag/Al_2O_3 in the presence of H_2. Consequently, NH_3 formed during the ethanol-SCR reaction could be able to act as a reducing agent itself and effectively reduce NO_x over Ag/Al_2O_3 when hydrogen is present in the feed. However, the content of NH_3 in the

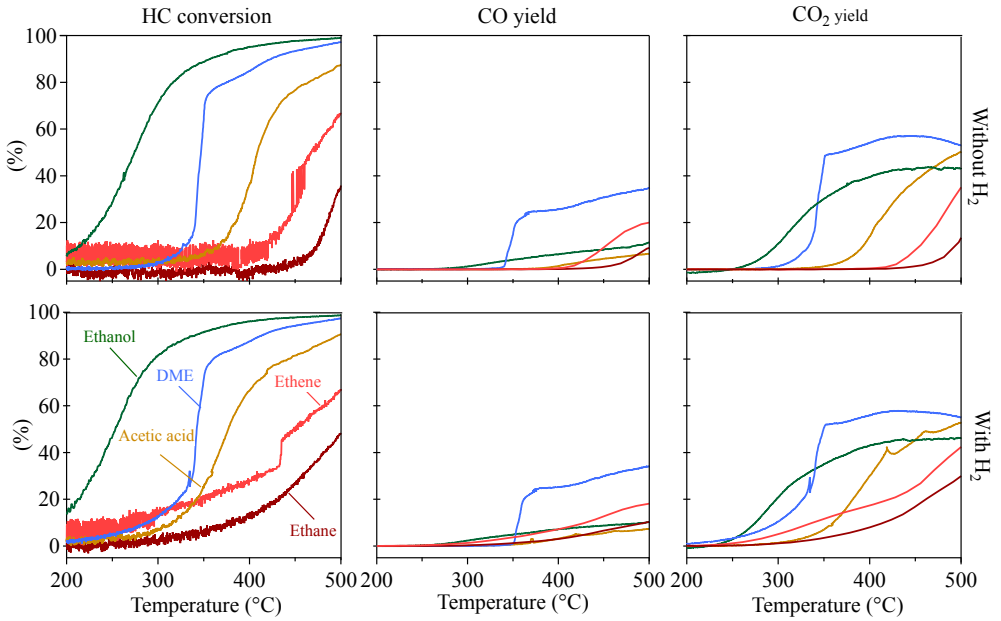

Figure 4.2: Conversion of the reductant (left), CO yield (middle) and CO_2 yield (right) during lean NO_x reduction over Ag/Al_2O_3. Reducing agents are ethane (dark red), ethene (light red), ethanol (green), acetic acid (orange) and DME (blue).

outflow seems unaffected by the presence of hydrogen, indicating that NH_3 is not consumed as a reductant to a large extent. This is in compliance with the findings by Pihl et al. [67]. Over the In/Al_2O_3 catalyst, lower amounts of NH_3 are detected during ethanol-SCR compared to over Ag/Al_2O_3. However, only half the amount of NH_3 is detected when H_2 is added to the feed, and since In/Al_2O_3 is inactive for NH_3-SCR in absence of hydrogen [55], this indicates that H_2-assisted NH_3-SCR may be part of the ethanol-SCR reaction over the In/Al_2O_3 catalyst (Paper I). Furthermore, almost 400 ppm ethene is detected during ethanol-SCR over In/Al_2O_3, peaking around 450 °C. Since In/Al_2O_3 is active for ethene-SCR in this temperature range, this may also be part of the ethanol-SCR reaction over In/Al_2O_3.

Among the C_2-based reducing agents, DME acts quite differently compared to the other reductants, showing a significantly higher activity for NO_x reduction over In/Al_2O_3 than Ag/Al_2O_3. Literature reports that DME undergoes gas phase radical reactions with NO, O_2 and H_2O, and thereby changing the gas phase composition significantly before reaching the catalyst [68]. Therefore, a catalyst suitable for DME-SCR should hold other properties than a conventional HC-SCR catalyst, such as avoiding further oxidation of the gas phase composition and possess high capability for NO_x reduction using ox-

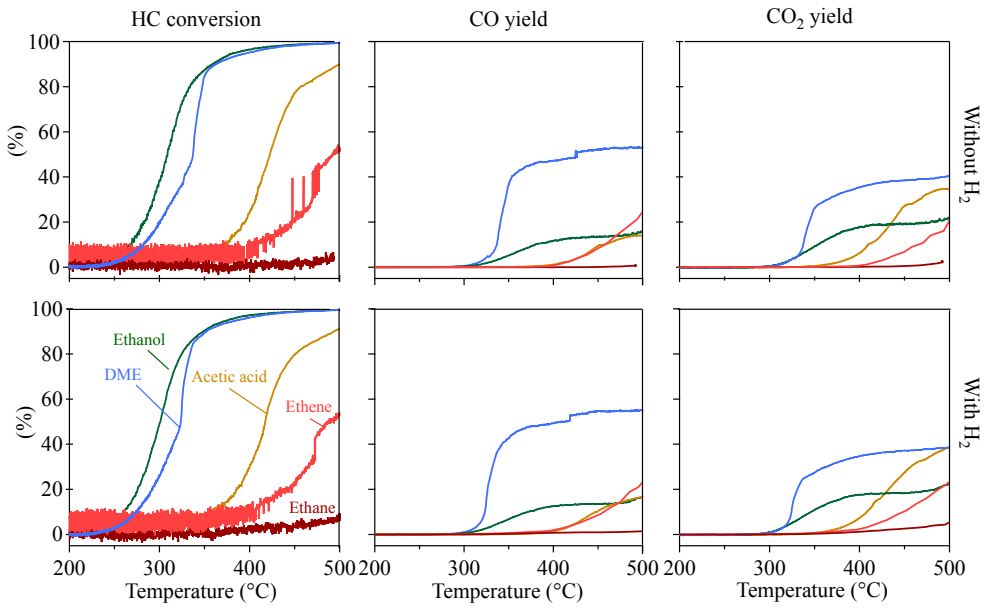

Figure 4.3: Conversion of the reductant (left), CO yield (middle) and CO_2 yield (right) during lean NO_x reduction over In/Al_2O_3. Reducing agents are ethane (dark red), ethene (light red), ethanol (green), acetic acid (orange) and DME (blue).

idized C_1-hydrocarbons [68]. Moreover, Table 4.1 shows that a significant amount of methanol is formed during DME-SCR over In/Al_2O_3. This is likely due to hydrolysis of DME over In/Al_2O_3:

$$H_3C\text{-}O\text{-}CH_3 + H_2O \longleftrightarrow 2\ H_3COH$$

The methanol formation is favored above 200 °C with less than stoichiometric amounts of water, whereas the major part of DME has already reacted in gas phase and is therefore no longer available for hydrolysis over the catalyst. Furthermore, it has also been reported that acidic sites are important for a highly active catalyst when reducing NO_x using DME [69]. The concentration of acidic sites was measured by NH_3-TPD, showing that the In/Al_2O_3 sample holds a higher concentration of acidic sites, compared to Ag/Al_2O_3. This could be a reason for the higher activity for DME-SCR over In/Al_2O_3 compared to Ag/Al_2O_3. Although un-impregnated Al_2O_3 holds an even higher density of acidic sites then In/Al_2O_3, it has been demonstrated that In/Al_2O_3 exhibits a higher activity for NO_x reduction with DME compared to In_2O_3 and γ-Al_2O_3 separately [70]. The results from the NH_3-TPD are presented and further discussed in section 4.2.

The byproduct yield of the experiments with H_2-assisted NH_3-SCR over

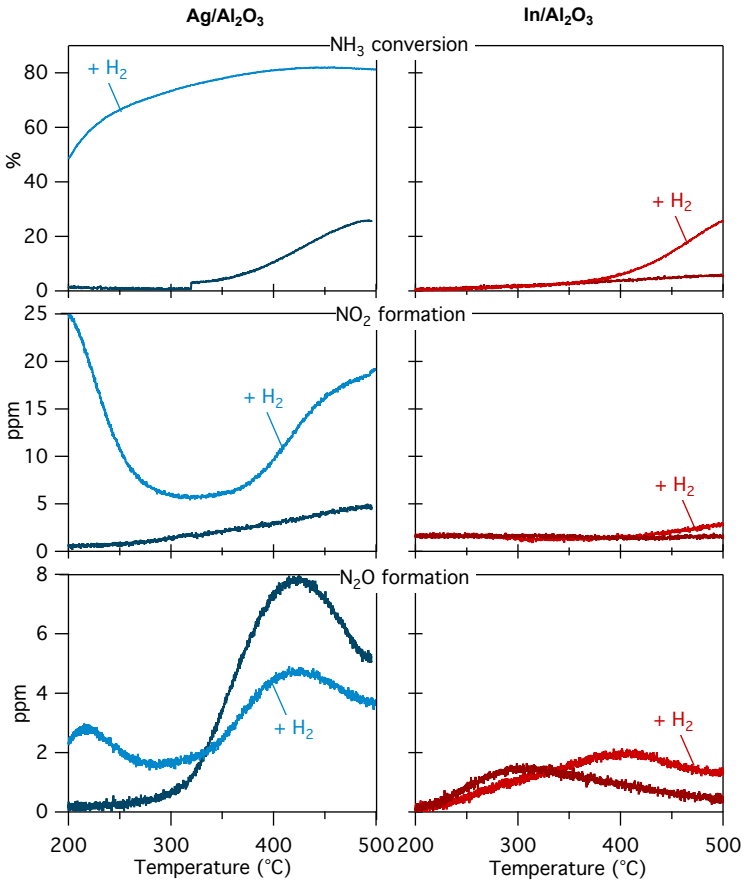

Figure 4.4: Conversion of NH_3 (top), NO_2 yield (middle) and N_2O yield (bottom) during NH_3-SCR over Ag/Al_2O_3 to the left and In/Al_2O_3 to the right.

Ag/Al_2O_3 and In/Al_2O_3 are shown in Figure 4.4, together with the conversion of the reducing agent. Over both catalysts, NH_3 does not convert when H_2 is absent, except for oxidation of NH_3 to NO at elevated temperatures, as mentioned earlier in this section. The N_2O yield over the Ag/Al_2O_3 catalyst is low and it is clear that H_2 suppresses the N_2O production over this catalyst, in accordance with literature [71].

In summary, the diversity in activity among these reductants demonstrates that the nature of the reducing agent is of uttermost importance when designing a successful catalytic system. During HC-SCR, the current work demonstrates that NO_x reduction varies as a function of the exact nature of the reductant, since despite that all HC reductants are based on two carbon atoms, the activity for NO_x reduction differs significantly over the same catalyst. Parameters such as activation (i.e. partial oxidation) ability of the hydrocarbon, which in turn depends on the nature of the C-H (or C-C) bonds, accessibility of π -electrons, molecular orientation (steric effects) and sticking probability of the reductant have been identified as critical factors [41, 72-75]. The effect of the oxidation state of the active phase on NO_x reduction is discussed in Section 4.3.1.

4.2 Influence of an uneven reductant dosage on NO_x reduction and slip of the reducing agent

The reductant in NH_3-SCR is typically supplied from urea, which decomposes to ammonia over the catalyst, see Figure 4.5 for a schematic illustration of a urea-SCR system. However, optimizing the spray setup is difficult and may result in uneven ammonia distribution, causing inefficient NO_x conversion and ammonia slip. A quantification and analysis of this issue is addressed in Paper III.

The degree of uneven distribution of ammonia to each individual catalyst channel in a hydrogen-assisted NH_3-SCR Ag/Al_2O_3 catalyst is evaluated for two different cases; with the injection spray situated in the center of the exhaust pipe or at the pipe wall. In this study, the results of the computational fluid dynamics (CFD) simulation by Lundström and Ström [76] were combined with a kinetic model developed by Tamm et al. [33], adapted to new experimental data. Gaussian probability distribution functions for the two cases of ammonia dosage are shown in Figure 4.6, where the probability that a catalyst channel receives a certain ammonia dose is plotted versus the

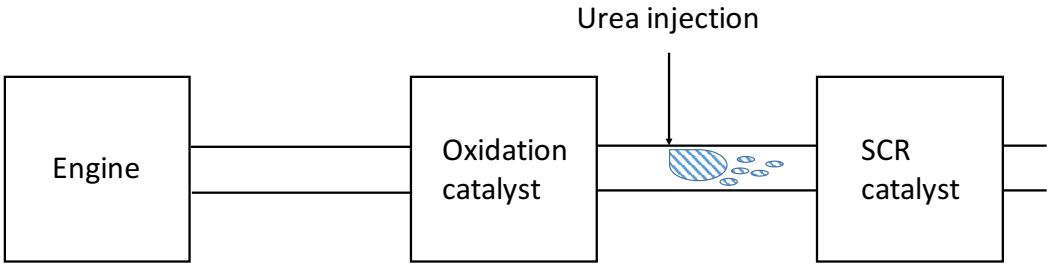

Figure 4.5: Illustration of a simplified diesel aftertreatment system with urea-SCR.

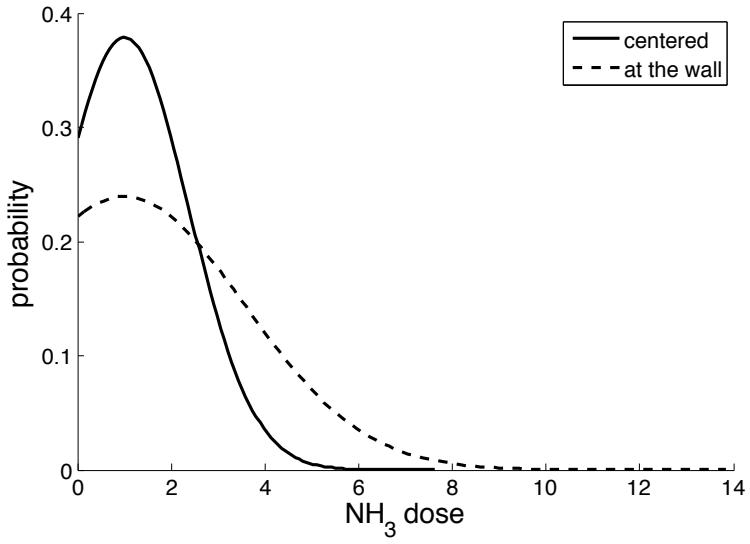

Figure 4.6: Probability distribution function of the NH_3 dose, where a NH_3 dose equal to 1 represents the stoichiometric dose.

range of doses seen in the raw data. The ammonia dose is here normalized by the average dose, so that an ammonia dose of two indicates that the channel in question receives twice the amount of ammonia that the average channel does. It is clear that the arrangement with the spray positioned in the center of the exhaust pipe produces more evenly distributed ammonia to the inlet of the catalyst than the arrangement with the spray originating from the exhaust pipe wall. However, both arrangements produce a large spread in the dose to the individual channel.

Figure 4.7 shows the NO conversion and the ammonia slip as functions of the normalized ammonia dose. These are calculated with the kinetic model using the input parameters of the Ag/Al_2O_3 catalyst described previously. It is assumed that an average dose implies dosing 500 ppm NH_3 (and 1000 ppm H_2) to reduce the 500 ppm NO, which is consistent with the fact that the global stoichiometry between NO:NH_3:H_2 is 1:1:2 during the SCR reactions [31]. The NO conversion increases rapidly with increasing dose from zero to unity, and then it increases another 10 percentage points up to a dose of approximately four times the average, after which no further improvement in NO conversion is observed with increasing ammonia dosage. However, the ammonia slip increases almost linearly above an ammonia dose equal to unity and reaches more than 4500 ppm for a channel that receives 10 times the average ammonia dose. For doses lower than unity, the ammonia slip is insignificant.

The average NO conversions and ammonia slips for the two spray arrangements depicted in Figure 4.7 are shown in Table 4.2. These values are calculated with the micro-kinetic model for the distribution of channel inlet conditions seen in the raw CFD data. It is shown that the global NO conversion is higher with the more evenly distributed ammonia concentration obtained for the centered spray arrangement. The largest differences are however observed for the ammonia slip, where the effect of local overdosing in the wall spray arrangement becomes apparent.

Although the NO reduction is almost maximized at stoichiometric conditions of NO and ammonia, the optimal ammonia dose is 0.83, as shown in Figure 4.8. In this illustration, it has been assumed that the environmental and health costs for releasing these two pollutants are weighted equally. This information is of importance when designing a urea-SCR system where an additional oxidation catalyst is not used, for example due to lack of space or when there is an increased risk of catalyst poisoning. In these cases, a sub-stoichiometric ammonia dose could be preferable to minimize the risk for ammonia slip.

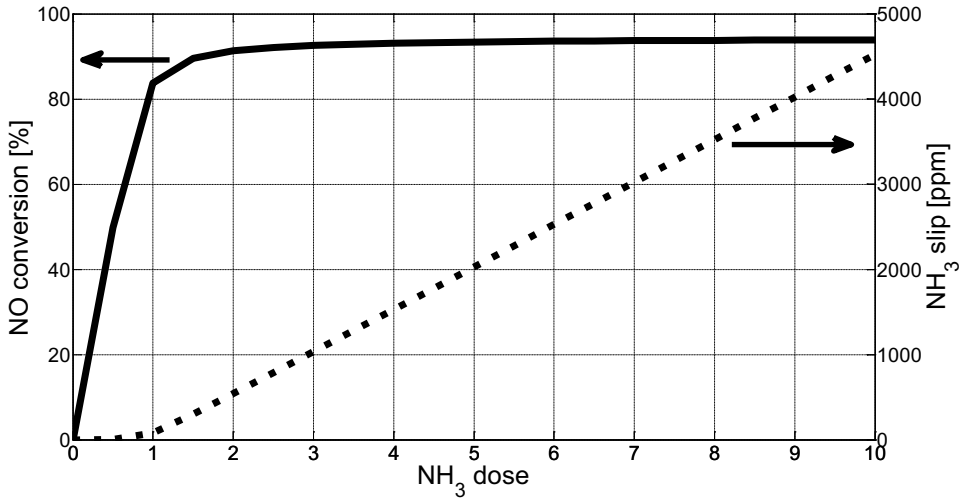

Figure 4.7: NO conversion (left axis) and NH_3 slip (right axis) as a function of the NH_3 dose in an individual catalyst channel at 300°C.

Table 4.2: NO conversion, NH_3 slip and the sum of NO and NH_3 slip (mean values) as a function of the urea-spray position.

Position	**NO conversion** [%]	**NH_3 slip** [*ppm*]	**NO + NH_3 slip** [*ppm*]
Center	61	300	495
Wall	52	565	805

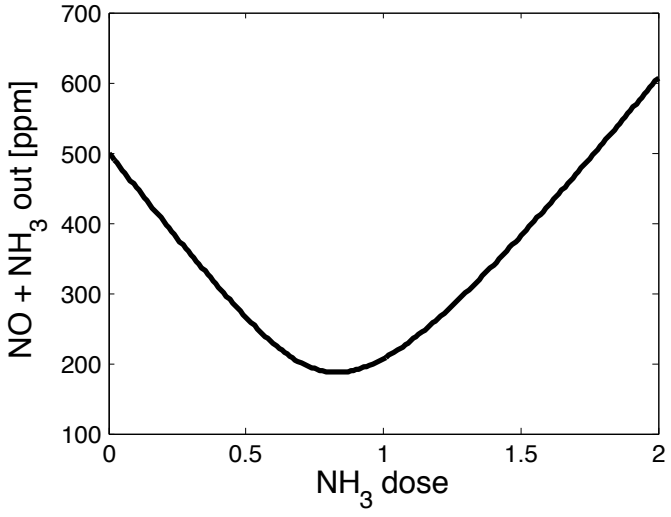

Figure 4.8: The sum of NO and ammonia slip as a function of the normalized ammonia dose to each channel.

4.3 The catalytically active sites

In order to exhibit a highly active catalyst, several criteria must be fulfilled. Among these are high surface area and a high distribution of the active phase. In this section, the surface properties of the Ag/Al_2O_3 catalyst is compared to an In/Al_2O_3 catalyst sample.

The specific surface area of the respective catalyst powder was measured by N_2-sorption according to the BET method. The bare alumina sample provides 197 m^2/g, and the surface area remained high after impregnation (188 and 185 m^2/g for In/Al_2O_3 and Ag/Al_2O_3, respectively). Furthermore, the X-ray diffractograms in Figure 4.9 shows that all patterns are characteristic to that of γ-Al_2O_3 and that no additional significant peaks that could be attributed to silver and indium crystalline particles larger than 3-5 nm [62] could be observed, confirming an even distribution of the active phases.

The alumina support consists of a combination of aluminum and oxygen ions and can hold twelve different configurations of OH groups, bearing slightly different net charges, consequently possessing different properties, such as variations in acidity [77, 78]. The concentration of acidic sites among the samples were determined by NH_3-TPD profiles, deconvoluted into gaussian peaks, showed in Figure 4.10. The variation of number and strength of acidic sites among the samples are clearly illustrated. In total, the highest

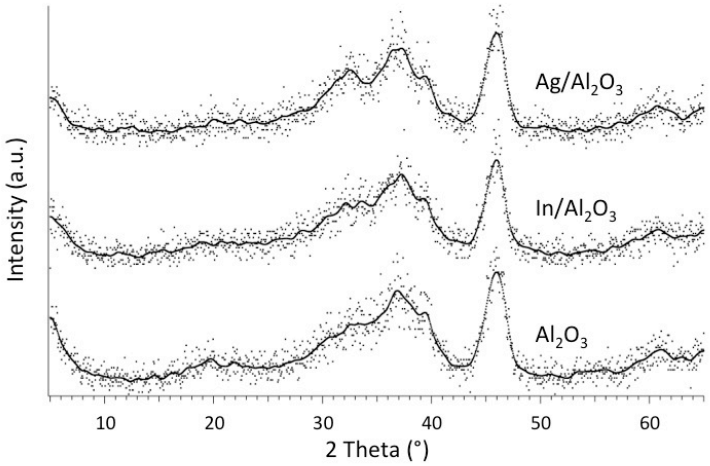

Figure 4.9: X-ray diffractograms of the Ag/Al_2O_3 and In/Al_2O_3 samples together with bare Al_2O_3.

concentration of acidic sites is found at the bare γ-Al_2O_3 sample, followed by In/Al_2O_3 and Ag/Al_2O_3, which possesses the lowest concentration of acidic sites as seen in Table 4.3. Furthermore, the weakest type of acidic site (i.e., the peak with lowest desorption temperature) can be found at a higher temperature for the bare γ-Al_2O_3 sample, corresponding to 19% of the total desorbed amount of NH_3, compared to the Ag/Al_2O_3 (49%) and In/Al_2O_3 (16%) samples, respectively. This peak is marked with a blue dotted line in the figure. The peak representing the strongest type of acidic site, i.e., the peak at the highest temperature, is marked with a red dotted line in the figure and is also found at a higher temperature for the γ-Al_2O_3 sample. In addition, the highest desorption-temperature peak of the impregnated samples is marked with a green dotted line in the figure and corresponds to the middle-temperature desorption peak of γ-Al_2O_3, indicating that the impregnation with silver and indium, respectively, results in loss of strong acidic sites. For the bare γ-Al_2O_3 sample, 33% of the total desorbed amount of NH_3 is adsorbed on this (strongest acidic) type of site, compared to 6% in the Ag/Al_2O_3 and 52% in the In/Al_2O_3 sample. However, the Gaussian peak representing the strongest acidic sites of the bare γ-Al_2O_3 sample is centered around almost 100 °C higher temperature compared to the peak holding the most acidic site of In/Al_2O_3. This implies that the impregnation procedure of γ-Al_2O_3 leads to an electronical modification and physical blockage of acidic sites at the catalyst support.

Table 4.3: Total desorbed amount of NH_3 during the NH_3-TPD experiments.

Sample	Desorbed NH_3 (mmol/cm^2)
γ-Al_2O_3	11.2
Ag/Al_2O_3	7.4
In/Al_2O_3	9.5

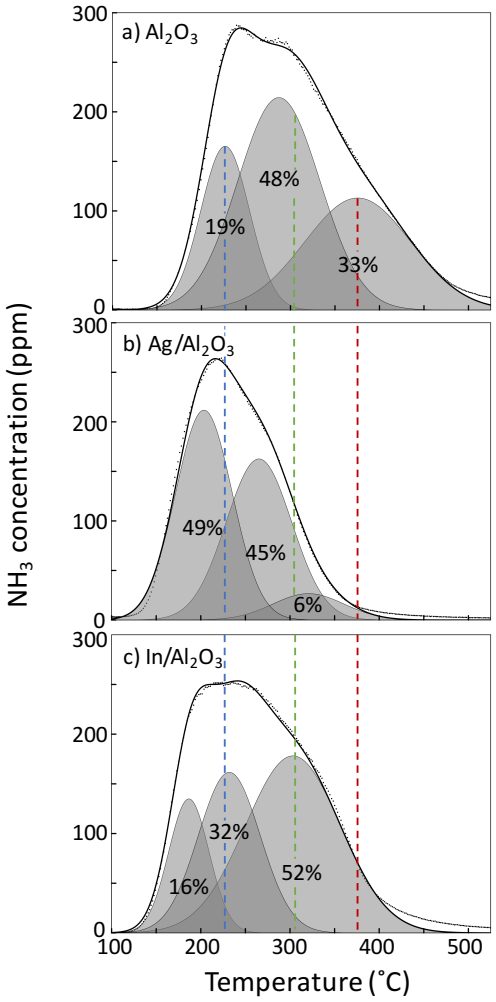

Figure 4.10: NH_3- temperature programmed desorption (TPD) profiles for (a) γ-Al_2O_3; (b) Ag/Al_2O_3 and (c) In/Al_2O_3, with the desorbed NH_3 concentration as a function of the temperature. The desorbed amount of NH_3 in the deconvoluted peaks are denoted in percentage of the measured total desorbed amount of NH_3.

4.3.1 Influence of gas phase composition

Metal oxidation state during NO_x reduction

Diffuse reflectance UV-vis spectroscopy was used for identification of the silver and indium species present in the catalyst samples. In order to investigate the influence of the hydrogen assistance during SCR experiments, the catalyst samples were pretreated in H_2 at 300 ℃ for 20 min prior to the UV-vis measurements. The resulting spectra of the alumina subtracted Ag/Al_2O_3 and In/Al_2O_3 samples are shown in Figure 4.11 The spectrum of the fresh (i.e. non-pretreated) Ag/Al_2O_3 catalyst (Figure 4.11a) shows that the sample contains a mixture of isolated Ag^+-ions, which exhibit absorption peaks at 192-250 nm [35,79-81], $Ag_n{}^{\delta+}$-clusters with peaks at 238-370 nm [79,82-84] and Ag^0 (metallic silver) with signals >390 nm [22, 35, 45, 79, 84-86]. After exposure to H_2, peaks increase in wavelengths corresponding to $Ag_n{}^{\delta+}$-clusters and Ag^0. However, isolated Ag^+-ions exhibiting peaks below 200 nm may also have been present in the samples without being detected, since the spectrum only contains signals above 200 nm due to instrument limitations [87]. Literature [37] acknowledges silver clusters as prime species for the activation of NH_3 in NH_3-SCR over Ag/Al_2O_3 and it has been shown that the activity is linearly proportional to the relative amount of these species [35]. The following reaction path for NO_x reduction was proposed: (*i*) dissociation of H_2 on the Ag site, (*ii*) spillover of H^+ to form a proton on Al_2O_3, (*iii*) aggregation of isolated Ag^+ ions to $Ag_n{}^{\delta+}$-clusters ($n \leq 8$), (*iv*) reduction of O_2 promoted by $Ag_n{}^{\delta+}$-clusters and H^+ to $O_2{}^+$, H_2O and $Ag_n{}^{(\delta+x)+}$ or Ag^+, (*v*) N–H activation by $O_2{}^-$ to yield NH_x ($x \leq 2$) (*vi*) oxidation of NO by $O_2{}^-$ forming NO_2, (*vii*) reaction between NH_x and NO to yield N_2 and H_2O [35]. During HC-SCR reactions, alkanes exhibits lower reactivity compared to alkenes, and it is assumed that $Ag_n{}^{\delta+}$-clusters provides active sites for alkane activation, which can be owing to that these clusters can polarize the saturated hydrocarbons and thereby facilitate partial oxidation of this reductant [23].

The UV-vis spectrum of fresh (i.e. non-pretreated) In/Al_2O_3 is shown in Figure 4.11b. Peaks in the range 200-450 nm are attributed to In_2O_3 [88-93]. The spectrum recorded after the H_2-pretreatment shows broadened absorption peaks with a slight redshift (see Figure 4.11d). Lv et al. [88] experienced that increased concentration of In_2O_3 results in a broadening and a redshift of the UV-vis absorbance edge. However, after H_2-pretreatment, peaks also increase slightly at longer wavelengths, i.e. >450 nm, which could represent an increased concentration of more reduced indium species. This indicates that the exposure of In/Al_2O_3 to H_2 could result in increased concentration

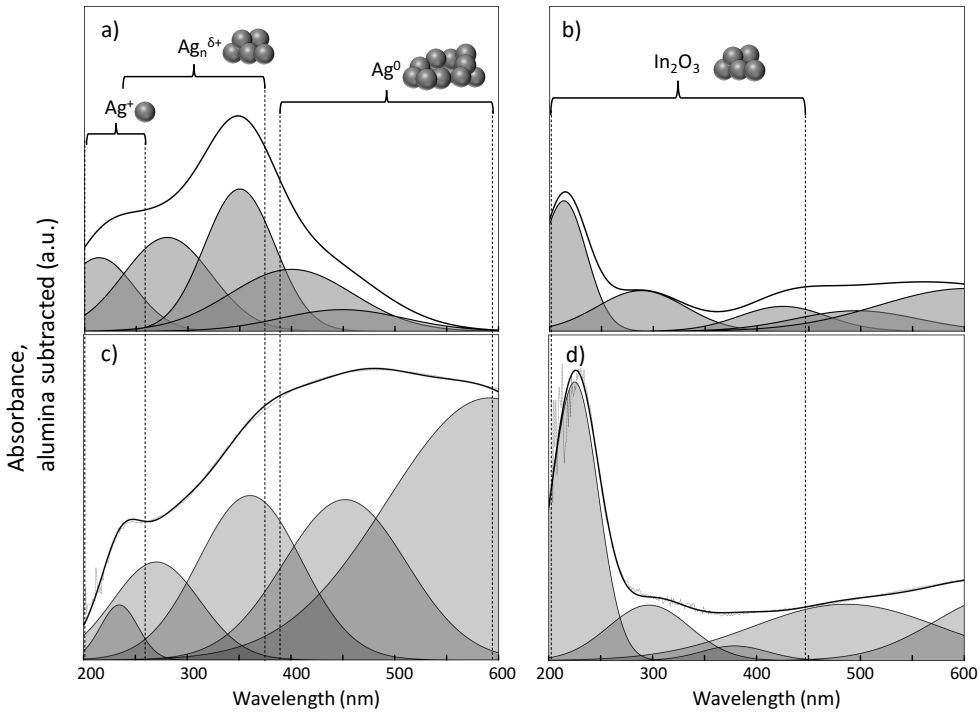

Figure 4.11: UV-vis spectra of Ag/Al_2O_3 (a and c) and In/Al_2O_3 (b and d) with the absorbance for the alumina sample subtracted, plotted as a function of the wavelength. The top spectra represent the fresh, i.e. unpretreated samples while the bottom spectra are after pretreatment in H_2 at 300 °C. The scale of the a and c, and b and d, respectively, are the same.

of species that are more reduced than In_2O_3. The reaction mechanism proposed for In/Al_2O_3 could therefore resemble what Shimizu et al. suggest for Ag/Al_2O_3, which could explain the promoting effect of H_2 during NH_3-SCR over In/Al_2O_3. However, NH_3-TPD profiles of the catalysts elucidate the difference in acidity. The stronger affinity between NH_3 and In/Al_2O_3 could possibly hinder proper activation of NH_3. Moreover, Park et al. [94] propose that dispersed In_2O_3 clusters promote the activation (i.e. partial oxidation) of HC that, with utilization of active alumina sites, selectively reduce NO_x to N_2 during HC-SCR. Hence, the promoting effect of hydrogen in HC-SCR could originate in increased formation of dispersed In_2O_3 clusters that, in turn, enable HC activation.

To sum up, H_2 seems to promote the formation of species that have been recognized to be important for the activation of the reducing agent, both over Ag/Al_2O_3 and In/Al_2O_3. Since the hydrogen effect has been shown to be rapidly reversible [7, 47], the influence of hydrogen on the metal oxidation state is likely not a single explanation for the remarkable increase of hydrogen on catalytic activity, but rather in combination with a more direct effect on the reaction mechanism.

Surface species during NO_x reduction

The catalyst surface is affected by the content of the surrounding gas environment. In order to connect the active phase to the catalyzed reaction, DRIFTS was used to follow the formation of surface species at reaction conditions during H_2-assisted NH_3-SCR. Figure 4.12 shows the formation of surface species for the Ag/Al_2O_3, In/Al_2O_3 and γ-Al_2O_3 samples after 10 min exposure to NO, NH_3, H_2 and O_2 at 300 °C. All detected peaks remained after the specific gas component that gave rise to the corresponding absorption band was switched off, indicating chemisorption of the surface species. Absorption bands assigned to the adsorption of NO and NH_3 are presented separately below.

Nitrate and nitrite surface species
Surface nitrate and nitrite species are formed upon exposure of Al_2O_3-based catalysts to NO and O_2 (or to NO_2). Nitrites have been recognized as an intermediate state in the formation of nitrates over Ag/Al_2O_3 [48], which may be a reason for the nitrite band to appear at 1228 cm^{-1} in the γ-Al_2O_3 and In/Al_2O_3 spectra, but being absent in the spectrum of Ag/Al_2O_3. Absorption bands related to the symmetric N=O stretching vibrations are located in the region between 1650 and 1500 cm^{-1}, while the asymmetrical stretching of

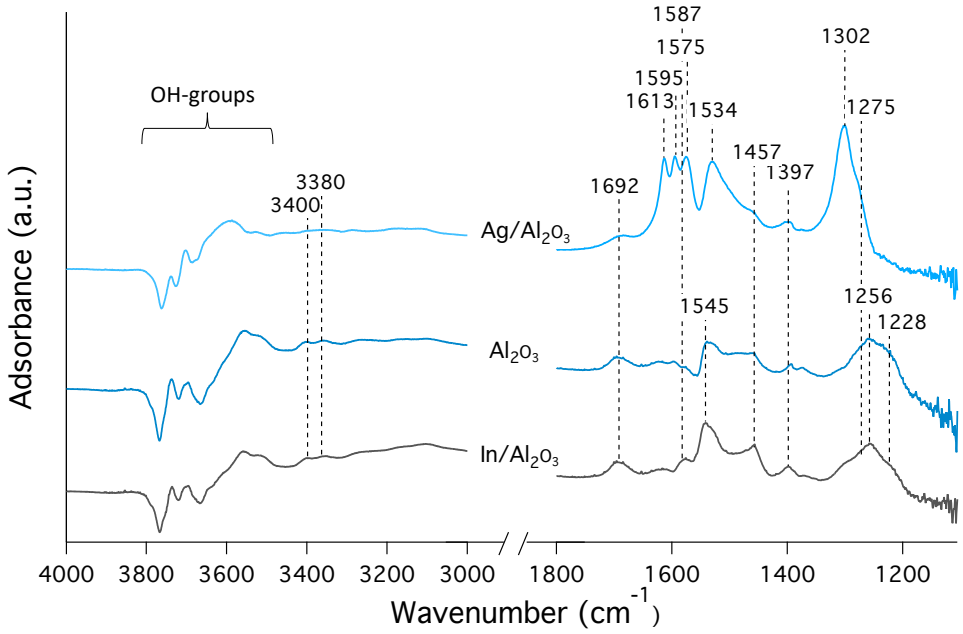

Figure 4.12: Diffuse reflectance infrared Fourier transform spectroscopy (DRIFTS) show formation of surface species for the Ag/Al_2O_3, In/Al_2O_3 and -Al_2O_3 samples during the exposure to selective catalytic reduction (SCR) reaction conditions (NO, NH_3, H_2, O_2, Ar-bal.) at 300 °C.

the O–N–O group can be detected between 1200 and 1350 cm^{-1} [26, 48, 95]. Broad peaks centered around 1256 cm^{-1} are located in the In/Al_2O_3 and γ-Al_2O_3 spectra, as shown in Figure 4.12. This band is assigned to (bidentate) nitrate [96]. In the same region, at 1302 cm^{-1}, Ag/Al_2O_3 exhibits a sharp peak, which is assigned to monodentate nitrate [48, 96]. The three peaks located at 1575, 1595 and 1613 cm^{-1} for the Ag/Al_2O_3 sample are assigned to bridged-, bidentate- and mono-dentate nitrate, respectively [48, 87]. In general, it should be noted that the Ag/Al_2O_3 sample exhibits both stronger and a wider variety of signals due to adsorption of nitrates and nitrites, compared to In/Al_2O_3.

Ammonia surface species
Brønstedt acidic sites adsorb NH_4^+ ions which result in the absorption bands at 1397 and 1692 cm^{-1} [97, 98]. Moreover, the symmetric and asymmetric vibration of surface coordinated NH_3 results in absorption bands at 1275 and 1587 cm^{-1}, respectively [98]. The less pronounced absorption bands at 3380 and 3400 cm^{-1} are assigned to the symmetric and asymmetric N–H stretching vibrations of NH_3 hydrogen bonded to surface OH [97, 99]. Absorbance bands assigned to NH_3-surface species are in general more pronounced over In/Al_2O_3 compared to Ag/Al_2O_3. This indicates that the adsorption of NH_3-surface species is more efficient over the former two samples compared to the latter, which is supported by the NH_3-TPD (which was discussed in the introduction of section 4.2), showing that the γ-Al_2O_3 and In/Al_2O_3 samples provide higher density of acidic sites, compared to the Ag/Al_2O_3 sample.

Hydroxyl groups
Absorption bands assigned to hydroxyl groups were observed at 3500–3800 cm^{-1} [100]. Comparing the relative peak intensities within the OH-band area of the infra-red patterns, it can be shown that the In/Al_2O_3 pattern resembles the one of γ-Al_2O_3 to a higher degree compared to Ag/Al_2O_3. Since alumina is impregnated with Ag and In in equivalent molar amounts, this implies that Ag affects the acidic properties of the OH-rich alumina surface to a higher degree compared to In, resulting in a lower concentration of acidic sites for Ag/Al_2O_3.

To sum up, during H_2-assisted NH_3-SCR conditions, the Ag/Al_2O_3 sample exhibits adsorption of NO-species in a wider variety compared to the In/Al_2O_3 sample. However, the latter adsorbes more NH_3-species compared to the former, confirmed by NH_3-TPD, which is discussed above. The strong adsorption of NH_3 at the In/Al_2O_3 sample may inhibit (self-poison) the NH_3 activation during SCR, thereby hindering further reaction over this catalyst.

4.4 Catalytically active nanosized alloys

The catalytic activity of bimetallic nanoparticles can differ significantly from those consisting of the respective elements [101], giving the opportunity to design catalysts holding specific, controllable properties [102, 103]. In order to synthesize such particles in homogenous size, the water pools of reversed microemulsions (w/o) can be used as nanosized reactors. In Paper IV, Pd-Ag nanoparticles were synthesized with this method, using methanol as reducing agent. Methanol is more environmental- and user friendly compared to hydrazine or sodium borohydride, which are commonly used for this type of synthesis. The nanoparticles were characterized with regards to crystallinity using XRD, elemental composition (core-shell or alloy structure) and catalytic activity using STEM-EDX, and CO adsorption and oxidation followed by *in situ* DRIFTS.

XRD diffractograms of nanoparticles supported on carbon are shown in Figure 4.13. The peaks at 44° arise from the carbon support and corresponds to C(100) [104-106]. The Ag sample exhibits peaks at 2θ = 38, 43, 64 and 77° which are assigned to the crystalline silver phases (111), (200), (220) and (311), respectively [107, 108]. The peaks of the Pd sample are detected at 2θ = 40, 46, 68, 78 and 79°, and are associated with the palladium crystal planes (111), (200), (220), (311) and (222), respectively, confirming the presence of face centered cubic structured Pd [105, 109-112]. The middle XRD-pattern that represents the 50/50 wt.% Ag/Pd mixture exhibits shifted peaks in between the Ag and Pd (111) phases, confirming the formation of a fcc-crystalline structured alloy [113, 114].

The elemental structure of the particle surface in relation to the overall particle composition (i.e. whether a core-shell structure or an alloy was formed) was investigated by using CO as a probe molecule in *in situ* DRIFTS. Figure 4.14a shows the absorption bands of CO adsorbed on the alumina-supported nanoparticles with different Ag/Pd compositions, ranging from 100 wt.% Pd to 100 wt.% Ag, with steps of 20%. Absorption peaks below 2000 cm^{-1} are attributed to the adsorption of bridge-bonded CO, and the bands above 2000 cm^{-1} are assigned to CO linearly bound to the surface [30, 115-119]. In agreement with literature [115, 116], CO does not adsorb onto Ag at the current conditions and following the behavior of the peaks change as a function of Pd-Ag content can therefore give an indication on the surface elemental structure. CO linearly bound to Pd is detected at 2099 cm^{-1} on the pure Pd sample, while the Ag-containing samples exhibit a weak redshift of this signal to lower wavenumber, relative the pure Pd sample (from 2099 to 2095

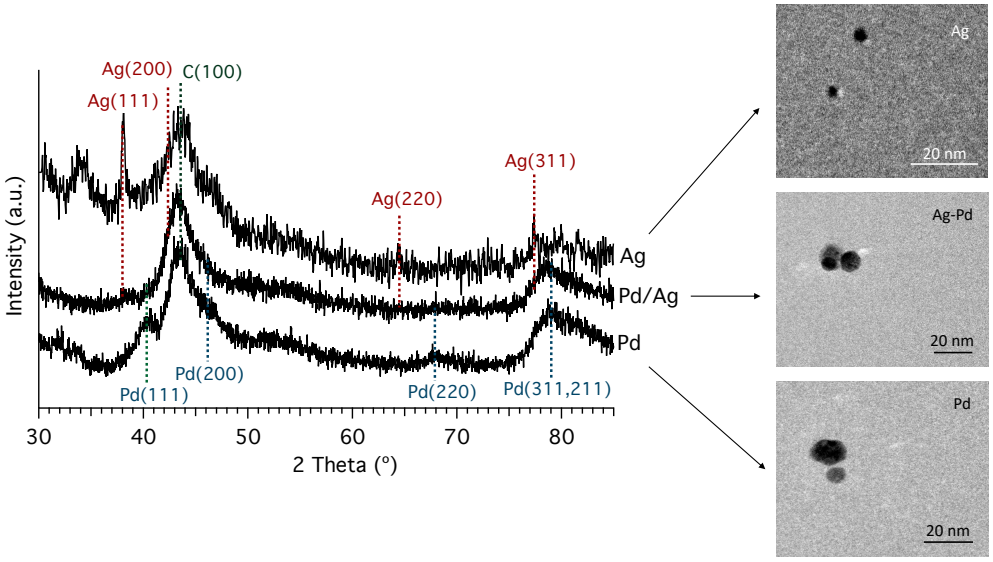

Figure 4.13: XRD patterns of the carbon-supported nanoparticle samples. The top pattern represents the 100% Ag particles, the middle a 50-50 wt.% mixture of Ag and Pd, and the bottom pattern represents the 100% Pd particles sample. To the right are the respective TEM images of the particles in the microemulsions.

cm^{-1}). Weaker adsorption of CO as a function of increased Ag content would however result in a blueshift of this signal towards the vibration signal of gas phase CO at 2143 cm^{-1}. Other effects such as change in dipole-dipole interaction between the linearly bound CO molecules should be responsible for this redshift [117, 120]. A significant decrease in peak intensity between for example 100% Pd and 80% Pd, 20% Ag could indicate that the surface composition of Ag is higher than the overall sample, pointing at the formation of a core-shell structure. The intensity of the linearly bound CO signal decrease gradually as the Ag content increase, indicating that the elemental content of the surface matches the content of the entire particle.

Moreover, the sample containing pure Pd particles exhibits a signal at 1960 cm^{-1}, showing the presence of bridge-bonded CO. According to Soma-Noto et al. [116], the diadsorbed bridge complex CO prevails on pure Pd. However, Childers et al. [121] show that the ratio between linearly bound and bridge-bonded CO on Pd strongly depends on particle size. In our study, the signal corresponding to the single-bonded CO vibrations is significantly more pronounced, compared to the bridge-bonded CO vibrations, also for the sample containing Pd only. The peak assigned to bridge-bonded CO exhibits a red shift (towards lower wavenumbers) as the silver content increases (from 1960 to 1930 cm^{-1}). If the nanoparticles would have higher Ag ratio at the

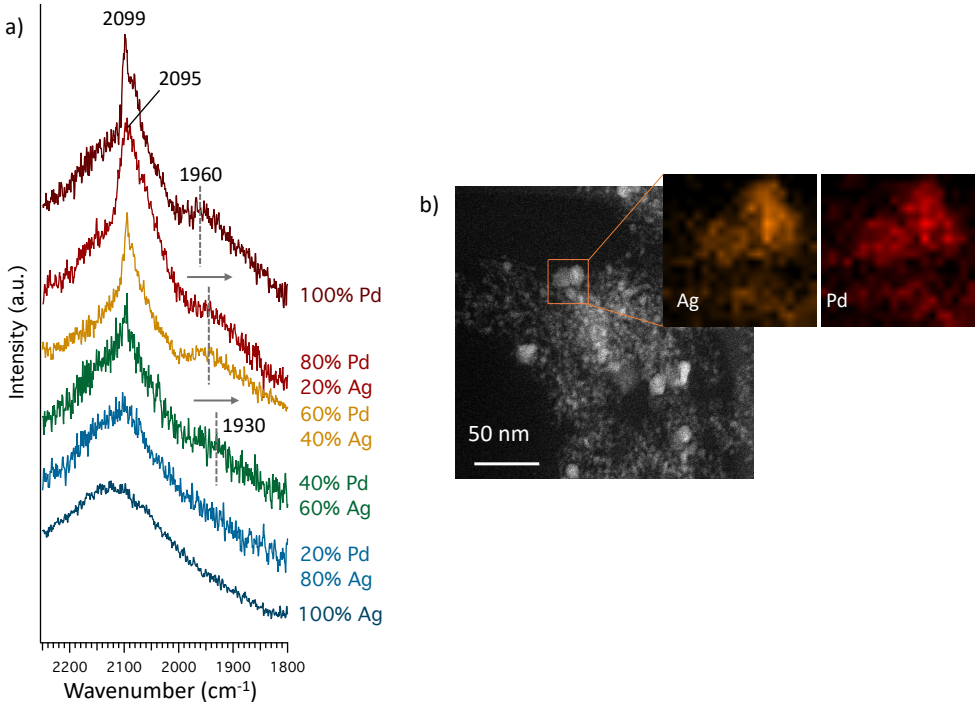

Figure 4.14: a) DRIFTS spectra showing chemisorbed CO at the Al_2O_3-supported nanoparticles, ranging from 100% Pd to 100% Ag with steps of 20 wt.%. b) STEM-EDX maps showing the location of Ag (orange) and Pd (red) in a nanoparticle.

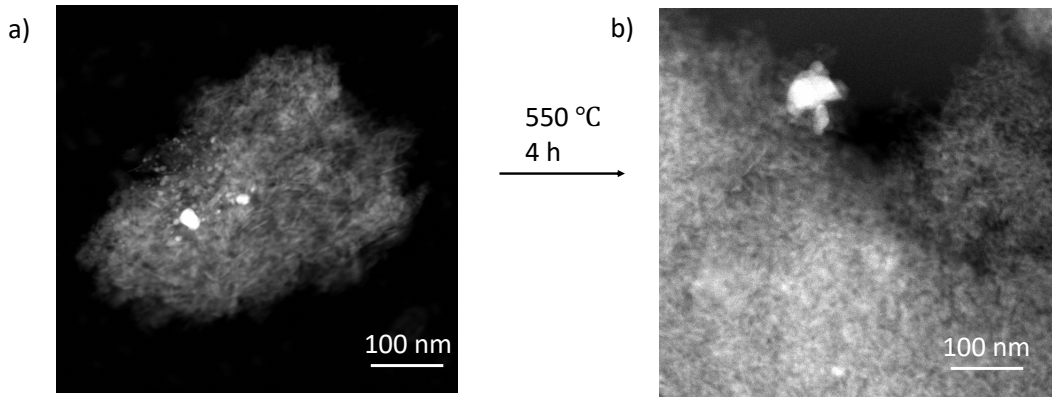

Figure 4.15: Al_2O_3-supported particles prior to (a) and after (b) calcination at 550 ℃.

surface, compared to the overall particle, the absorbance corresponding to bridge-bonded CO would decrease rapidly with increased Ag ratio, since each bridge-bonded CO molecule needs to occupy two surface Pd atoms. A Pd-prevailed surface would, on the other hand, result in similar CO absorbance regardless of Ag concentration, since the Ag core would not affect the CO adsorbed at the surface. The gradual redshift of the bridge-bonded CO, with increasing Ag ratio, might be due to electronic and/or geometric impact of Ag atoms in the Pd lattice. A particle surface with agglomeration of Ag and Pd atoms separately should only result in a gradual decrease of this signal, since the Pd lattice would not be affected. In summary, the results of the CO adsorption study indicate that the surface of the particles consists of the same Pd-Ag ratio as the entire particle, i.e. no core-shell structure can be detected. This is also illustrated in Figure 4.14b, showing the STEM-EDX mapping of a particle containing equal amounts of Pd and Ag, confirming an even distribution of the elements throughout the nanoparticles.

As shown in Figure 4.14, the size of the particles in the microemulsion solution is around 5-12 nm while the size of the alumina-supported particles is somewhat larger, as shown in Figure 4.15a. After calcination at 550 ℃, the particle size increase further (Figure 4.15b).

The DRIFTS spectra of CO oxidation over the alumina-supported nanoparticles are shown in Figure 4.16, with the particle content ranging from 100% Pd at the left to 20% Pd and 80% Ag to the right. The temperature ranges from 25 ℃ at the bottom to 400 ℃ at the top. The presence of gas-phase CO is represented by the double peaks around 2150 cm^{-1}, while the peaks evolving around 2350 cm^{-1} are due to formation of CO_2 [122]. The spectra show that the formation of CO_2 starts at a lower temperature over the sam-

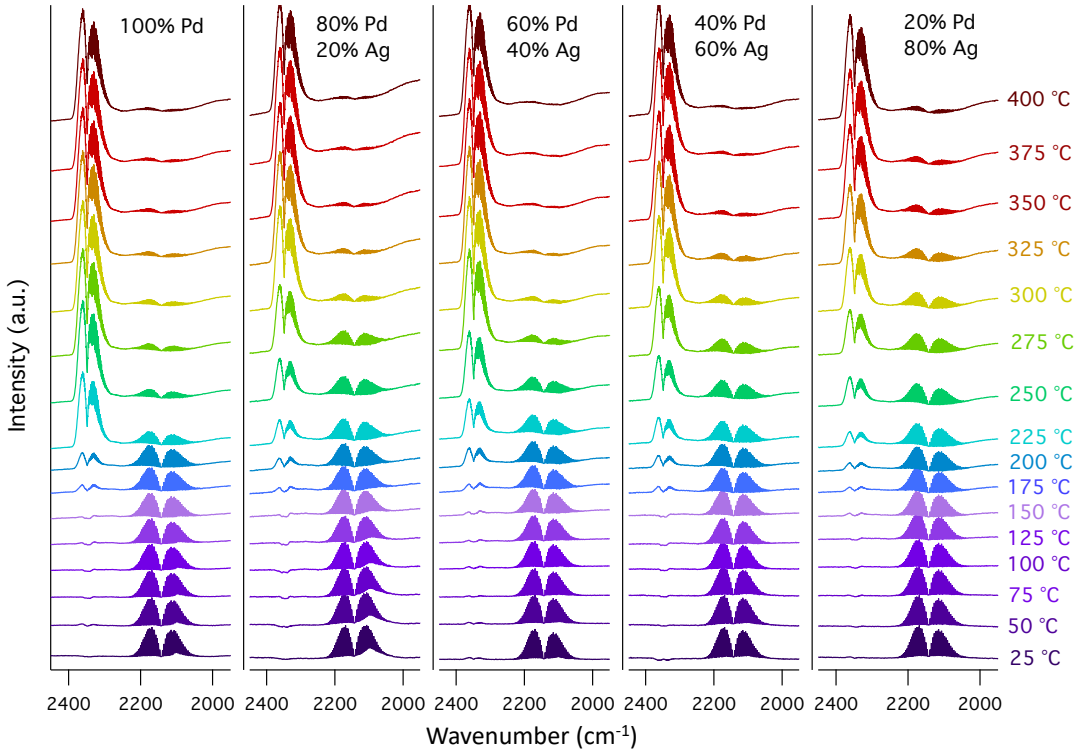

Figure 4.16: DRIFTS spectra of CO oxidation over Al_2O_3-supported Ag/Pd nanoparticles of varying ratios. The inlet gas composition was 0.5 vol.% CO and 2.5 vol.% O_2 (Ar-bal.)

ple containing pure Pd nanoparticles, as illustrated by the stronger CO_2/CO signal (light blue spectrum at 225 °C) for the pure Pd sample, compared to the other samples. Furthermore, the amount of chemisorbed CO (at 25 °C), is higher for the samples with high Pd content, compared to the samples containing more Ag. This absorption peak is located at 2098 cm^{-1} in these spectra and is overlapped by the right part of the gas phase-CO double peak. Moreover, the spectra representing the high ratio of Ag-samples exhibit lower CO oxidation at high temperature.

Figure 4.17 shows the simulated formation of approximately 2,000 nanoparticles from the initial droplet distribution. The core of the particles consists of either silver or palladium with a probability matching the proportions in the microemulsion mixture. Moving from the center of the particle towards the surface, the composition is gradually more mixed, indicating formation of alloys rather than core-shell structures. The average composition for the nanoparticles also corresponds to the proportions in the mixture, indicating

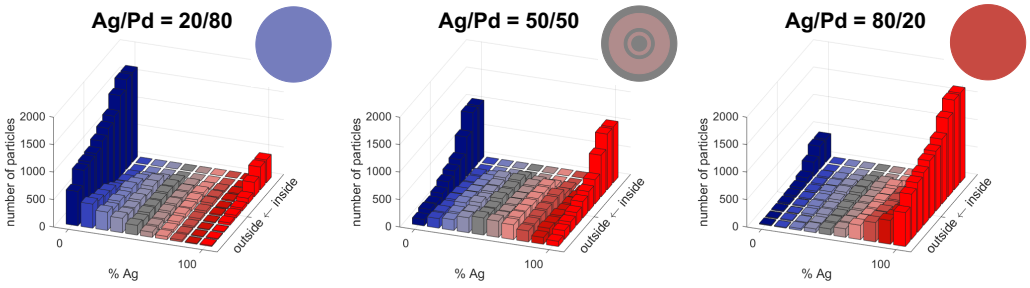

Figure 4.17: Simulation result histograms for the spatial data on Ag/Pd-nanoparticles for three different Ag/Pd-wt. ratios (from left to right: 20/80, 50/50 and 80/20). The colored spheres represent the average composition. Pd is represented in blue, Ag in red and a 50/50 mixture in grey. As the color turns to lighter tonalities, the proportion of the corresponding pure metal is higher.

minimal tendency to metal segregation. It can be concluded from the simulations that the particles synthesized from the microemulsions are alloys with both metals present at the particle surface in the equal proportions as the entire particle.

In summary, in the reversed microemulsion templated synthesis, the metal salts were reduced by the methanol into crystalline particles, which was shown by XRD measurements. Results provided by STEM-EDX, DRIFTS and the numeric simulations all show that the particles formed in this synthesis exhibit an alloy structure with the Ag and Pd atoms mixed, regardless of the Ag/Pd-ratio. Furthermore, the particles were shown to be active for CO oxidation, where the pure Pd-particle sample was active at a lower temperature, compared to the other ratios.

Chapter 5

Conclusions

Climate change motivate the use of more fuel efficient engines in the vehicles, which emit less of the green house gas CO_2 per driven kilometer. However, NO_x, which is poisonous to both humans and the environment, is more challenging to reduce in lean conditions, since the three-way catalyst is ineffective in excess oxygen.

In this work, Ag/Al_2O_3 has been evaluated as an SCR catalyst with C_2-hydrocarbons as well as ammonia as reducing agents, in order to investigate the active sites and elucidate the influence of the nature of the reducing agent during lean NO_x reduction. In particular, the work focus on how the catalytically active phases are affected by the SCR environment, and how the formed surface species interact with these phases.The Ag/Al_2O_3 catalyst was compared to an In/Al_2O_3 catalyst, containing the equivalent molar amount of active phase in order to investigate the role of the active phase. The effect of an uneven distribution of the reducing agent is also evaluated. Finally, this work investigates the possibility to form catalytically active bimetallic Pd-Ag nanoparticles, synthesized in the water pools of a reversed microemulsion using methanol as reducing agent for the metal complexes.

The results from the SCR experiments show that the Ag/Al_2O_3 catalyst in general exhibits superior activity for NO_x reduction compared to In/Al_2O_3. However, In/Al_2O_3 shows significantly higher activity with DME as the reductant, which may be explained by gas-phase radical formation that DME experiences together with the more pronounced ability of HC activation (i.e. partial oxidation) that Ag/Al_2O_3 exhibits. The 'hydrogen effect' observed over the Ag/Al_2O_3 sample may be explained by modification of surface species acquired after hydrogen exposure, resulting in increased concentration of $Ag_n^{\delta+}$-clusters. Such clusters have previously been identified as key components in the reaction mechanisms, both during HC- and NH_3-SCR.

Furthermore, the results show that in addition to Ag/Al_2O_3, In/Al_2O_3 also exhibits a 'hydrogen effect' during both HC- and NH_3-SCR. Hydrogen exposure of In/Al_2O_3 results in an increased number of In_2O_3 species, which have been identified as an active component for HC activation during HC-SCR. However, more reduced species are also formed during hydrogen exposure, which may be an explanation of the promoting effect of hydrogen during NH_3-SCR over this catalyst. Moreover, the hydrogen effect has been shown to be rapidly reversible when the hydrogen is removed from the gas feed. It is likely that the origin of this phenomenon is dual and a direct participation of hydrogen in the NO_x reduction reaction mechanism is feasible.

DRIFTS show that NO-species are formed to a higher extent over Ag/Al_2O_3 during SCR conditions, compared to In/Al_2O_3. The latter provide higher density of acidic sites, quantified by NH_3-TPD, and also exhibit higher NH_3 adsorption. Since adsorption of reactants in suitable proportions is crucial for high catalytic activity, an important difference between the two catalysts could be the stronger affinity for NH_3 over In/Al_2O_3, compared to Ag/Al_2O_3. This can possibly inhibit the NH_3 activation over the former, and thereby hindering further reaction over this catalyst, which is also shown by the lower SCR activity, compared to Ag/Al_2O_3.

Quantification of the NO reduction and ammonia slip in different locations of the reductant injection spray shows that the probability of an ammonia dose equal to unity is higher when the spray is positioned in the center of the exhaust pipe, compared to at the pipe wall. However, both arrangements produce a large spread in the ammonia dose to the individual catalyst channels. Furthermore, the NO conversion increases rapidly with increasing ammonia dose from zero to unity, and then it increases another 10 percentage points up to a dose of approximately four times the average, after which no further improvement in NO conversion is observed with increasing ammonia dosage. However, the ammonia slip increases almost linearly above an ammonia dose equal to unity and reaches more than 4500 ppm for a channel that receives 10 times the average ammonia dose. For doses lower than unity, the ammonia slip is insignificant.

Moreover, it was confirmed that catalytically active crystalline nano-alloys, which can hold properties that significantly differs from those of each element separate, could be synthesized by a simple route using methanol as an environmental friendly reducing agent. Following the CO-adsorption at particles of different Pd-Ag ratios by *in situ* DRIFTS indicates that the surface of the formed particles consists of equal Pd-Ag ratio as the entire particle,

i.e. no core-shell structure can be detected. The alloy structure could also be confirmed by STEM-EDX as well as in numeric simulations. In addition, CO oxidation experiments confirms that the particles are catalytically active.

This work contributes to the overall understanding of the interplay between various reducing agents and active sites in SCR of NO_x. The results presented in this thesis may therefore help advance current technologies to improve the sustainability of future transport solutions.

Acknowledgements

This work is funded by the Swedish Research Council and was performed within the Competence Centre for Catalysis, which is hosted by Chalmers University of Technology and financially supported by the Swedish Energy Agency and the member companies: AB Volvo, ECAPS AB, Johnson Matthey AB, Preem AB, Scania CV AB, Umicore Denmark ApS and Volvo Car Corporation AB

I would also like to thank:

Professor Hanna Härelind for giving me the opportunity to do my Ph.D. in this group and for being such an amazing supervisor and a great mentor.

My examiner **Professor Magnus Skoglundh** and co-supervisor **Prof. Per-Anders Carlsson** for all the support and guidance.

Ann Jakobsson and **Frida Andersson** for all the administrative help.

Stefan Gustafsson at CMAL for helping me with the TEM.

Hannes, Marika and **Freddy** for all the help in the help in the beginning of my Ph.D.

Anna and **Alexander** for helping me with experimental techniques.

All former and present colleagues at **TYK** and **KCK** for all the fun over the years.

My family for all the support.

Last but not least, my husband **Henrik** and our wonderful girls **Tove** and **Alice** for making me so happy. I love you so much!

Bibliography

[1] U.S.E.P. Agency, Clean air act requirements and history, http://www.epa.gov, recieved 2015-08-13.

[2] I. Chorkendorff, J.W. Niemantsverdriet, Concepts of modern catalysis and kinetics, WILEY-VCH Verlag GmbH & Co. KGaA, Weinheim, 2007.

[3] Eurostat Emissions of nitrogen oxides by source sector, ec.europa.eu/eurostat Accessed 2017-11-21.

[4] Dieselnet, http://www.dieselnet.com, Accessed 2017-12-03

[5] K. Arve, L. Capek, F. Klingstedt, K. Eranen, L.E. Lindfors, D.Y. Murzin, J. Dedecek, Z. Sobalik, B. Wichterlova, Top. Catal. 30-1 (2004) 91-95.

[6] J.P. Breen, R. Burch, C. Hardacre, C.J. Hill, J. Phys. Chem. B 109 (2005) 4805-4807.

[7] J.P. Breen, R. Burch, Top. Catal. 39 (2006) 53-58.

[8] H. Kannisto, H.H. Ingelsten, M. Skoglundh, J. Mol. Catal. A: Chem. 302 (2009).

[9] T. Miyadera, Appl. Catal., B. 16 (1998) 155-164.

[10] T. Nakatsuji, R. Yasukawa, K. Tabata, K. Ueda, M. Niwa, Appl. Catal., B. 17 (1998) 333-345.

[11] P. Granger, V.I. Parvulescu, Chem. Rev. 111 (2011) 3155-3207.

[12] M. Bowker, The Basis and Applications of Heterogeneous Catalysis, Oxford Science Publications, 1998.

[13] M.V. Twigg, Catal. Today 163 (2011) 33-41.

[14] R. Burch, Catal. Rev. -Sci. Eng. 46 (2004) 271-333.

[15] Z.M. Liu, S.I. Woo, Catal. Rev. -Sci Eng 48 (2006) 43-89.

[16] W.S. Epling, L.E. Campbell, A. Yezerets, N.W. Currier, J.E. Parks, Catal. Rev. -Sci. Eng. 46 (2004) 163-245.

[17] S. Matsumoto, Y. Ikeda, H. Suzuki, M. Ogai, N. Miyoshi, Appl. Catal., B. 25 (2000) 115-124.

[18] R. Burch, J.P. Breen, F.C. Meunier, Appl. Catal., B. 39 (2002) 283-303.

[19] R. Brosius, K. Arve, M.H. Groothaert, J.A. Martens, J. Catal. 231 (2005) 344-353.

[20] T. Maunula, Y. Kintaichi, M. Inaba, M. Haneda, K. Sato, H. Hamada, Appl. Catal., B. 15 (1998).

[21] K. Eranen, F. Klingstedt, K. Arve, L.E. Lindfors, D.Y. Murzin, J. Catal. 227 (2004) 328-343.

[22] K. Shimizu, J. Shibata, H. Yoshida, A. Satsuma, T. Hattori, Appl. Catal., B. 30 (2001).

[23] K. Shimizu, A. Satsuma, Phys. Chem. Chem. Phys. 8 (2006) 2677-2695.

[24] V.A. Sadykov, S.L. Baron, V.A. Matyshak, G.M. Alikina, R.V. Bunina, A.Y. Rozovskii, V.V. Lunin, E.V. Lunina, A.N. Kharlanov, A.S. Ivanova, S.A.

[25] K. Shimizu, M. Takamatsu, K. Nishi, H. Yoshida, A. Satsuma, T. Tanaka, S. Yoshida, T. Hattori, J. Phys. Chem. B 103 (1999).

[26] F.C. Meunier, J.P. Breen, V. Zuzaniuk, M. Olsson, J.R.H. Ross, J. Catal. 187 (1999) 493-505.

[27] C. Ciardelli, I. Nova, E. Tronconi, D. Chatterjee, T. Burkhardt, M. Weibel, Chem. Eng. Sci. 62 (2007) 5001-5006.

[28] C. Petitto, G. Delahay, J. Environ. Sci. 65 (2018) 246-252.

[29] K.-i. Shimizu, A. Satsuma, Appl. Catal., B. 77 (2007) 202-205.

[30] E.C. Adams, M. Skoglundh, M. Folic, E.C. Bendixen, P. Gabrielsson, P.-A. Carlsson, Appl. Catal., B, 165 (2015) 10-19.

[31] E.C. Adams, M. Skoglundh, P. Gabrielsson, P.A. Carlsson, Top. Catal., 59 (2016) 970-975.

[32] F. Klingstedt, K. Arve, K. Eranen, D.Y. Murzin, Acc. Chem. Res. 39 (2006).

[33] T. Miyadera, Appl. Catal., B. 2 (1993) 199-205.

[34] S. Tamm, S. Fogel, P. Gabrielsson, M. Skoglundh, L. Olsson, Appl. Catal., B. 136 (2013) 168-176.

[35] K.-i. Shimizu, A. Satsuma, J. Phys. Chem. C 111 (2007) 2259-2264.

[36] S. Tamm, L. Olsson, S. Fogel, P. Gabrielsson, M. Skoglundh, AIChE J. 59 (2013) 4325-4333.

[37] L. Yu, Q. Zhong, S. Zhang, Phys. Chem. Chem. Phys. 16 (2014) 12560-12566.

[38] L. Zhang, C. Zhang, H. He, J. Catal., 261 (2009) 101-109.

[39] K. Masuda, K. Tsujimura, K. Shinoda, T. Kato, Appl. Catal., B. 8 (1996).

[40] T. Miyadera, Appl. Catal., B. 13 (1997) 157-165.

[41] H. Harelind, F. Gunnarsson, S.M.S. Vaghefi, M. Skoglundh, P.-A. Carlsson, ACS Catal 2 (2012) 1615-1623.

[42] T.E. Hoost, R.J. Kudla, K.M. Collins, M.S. Chattha, Appl. Catal., B. 13 (1997) 59-67.

[43] L.E. Lindfors, K. Eranen, F. Klingstedt, D.Y. Murzin, Top. Catal. 28 (2004) 185-189.

[44] T. Chaieb, L. Delannoy, G. Costentin, C. Louis, S. Casale, R.L. Chantry, Z.Y. Li, C. Thomas, Appl. Catal., B. 156 (2014) 192-201.

[45] N. Bogdanchikova, F.C. Meunier, M. Avalos-Borja, J.P. Breen, A. Pestryakov, Appl. Catal., B. 36 (2002) 287-297.

[46] J. Shibata, Y. Takada, A. Shichi, S. Satokawa, A. Satsuma, T. Hattori, J. Catal. 222 (2004) 368-376.

[47] S. Satokawa, Chem. Lett. (2000) 294-295.

[48] S. Tamm, N. Vallim, M. Skoglundh, L. Olsson, J. Catal. 307 (2013) 153-161.

[49] H. Kannisto, H.H. Ingelsten, M. Skoglundh, Top. Catal. 52 (2009).

[50] N.A. Sadokhina, D.E. Doronkin, G.N. Baeva, S. Dahl, A.Y. Stakheev, Top. Catal. 56 (2013) 737-744.

[51] C. Thomas, Appl. Catal., B. 162 (2015) 454-462.

[52] P.S. Kim, M.K. Kim, B.K. Cho, I.-S. Nam, S.H. Oh, J. Catal. 301 (2013) 65-76.

[53] S. Satokawa, J. Shibata, K. Shimizu, S. Atsushi, T. Hattori, Appl. Catal., B. 42 (2003) 179-186.

[54] R. Burch, J.P. Breen, C.J. Hill, B. Krutzsch, B. Konrad, E. Jobson, L. Cider, K. Eranen, F. Klingstedt, L.E. Lindfors, Top. Catal. 30-1 (2004) 19-25.

[55] D.E. Doronkin, S. Fogel, S. Tamm, L. Olsson, T.S. Khan, T. Bligaard, P. Gabrielsson, S. Dahl, Appl. Catal., B. 113 (2012) 228-236.

[56] J. Ross, Heterogeneous Catalysis, Elsevier (2012) J.H. Li, J.M. Hao, X.Y. Cui, L.X. Fu, Catal. Lett. 103 (2005).

[57] A. Iglesias-Juez, A.B. Hungria, A. Martinez-Arias, A. Fuerte, M. Fernandez-Garcia, J.A. Anderson, J.C. Conesa, J. Soria, J. Catal., 217 (2003).

[58] K. Holmberg, B. Jönsson, B. Kronberg, B. Lindaman, Surfactants and Polymers in Aqueous Solutions, Second edition ed., John Wiley sons (2003).

[59] S. Brunauer, P.H. Emmett, E. Teller, J. Am. Chem. Soc. 60 (1938) 309-319.

[60] K.S.W. Sing, Adv. Colloid Interface Sci. 76 (1998) 3-11.

[61] G. Leofanti, M. Padovan, G. Tozzola, B. Venturelli, Catal. Today 41 (1998) 207-219.

[62] J.R. Anderson, K.C. Pratt, Introduction to characterization and testing of catalysts, Academic Press Inc., University of Melbourne, Australia, (1985).

[63] L. Cademartiri, O. Geoffrey A., Concepts of Nanochemistry, Wiley-VCH, Weinheim, (2009).

[64] I. Chorkendorff, H. Niemantsverdriet, Concepts of Modern Catalysis and Kinetics, Wiley-VCH, Weinheim (2003).

[65] C. Wang-Hansen, C.J. Kamp, M. Skoglundh, B. Andersson, P.-A. Carlsson, J. Phys. Chem. C 115 (2011) 16098-16108.

[66] M. Richter, R. Fricke, R. Eckelt, Catal. Lett., 94 (2004) 115-118.

[67] J.A. Pihl, T.J. Toops, G.B. Fisher, B.H. West, Catal. Today, 231 (2014) 46-55.

[68] S. Tamm, H.H. Ingelsten, M. Skoglundh, A.E.C. Palmqvist, Appl. Catal. B. 91 (2009).

[69] S.G. Masters, D. Chadwick, Appl. Catal. B., 23 (1999) 235-246.

[70] S. Erkfeldt, M. Petersson, A. Palmqvist, Appl.Catal. B., 117 (2012) 369-383.

[71] V.A. Kondratenko, U. Bentrup, M. Richter, T.W. Hansen, E.V. Kondratenko, Appl. Catal., B. 84 (2008) 497-504.

[72] M. Haneda, Y. Kintaichi, N. Bion, H. Hamada, Appl. Catal. B. 42 (2003).

[73] M. Haneda, E. Joubert, J.C. Menezo, D. Duprez, J. Barbier, N. Bion, M. Daturi, J. Saussey, J.C. Lavalley, H. Hamada, J. Mol. Catal. A., 175 (2001).

[74] J.A. Perdigon-Melon, A. Gervasini, A. Auroux, J. Catal., 234 (2005).

[75] T. Maunula, Y. Kintaichi, M. Haneda, H. Hamada, Catal. Lett., 61 (1999).

[76] A. Lundström, H. Ström, In:Sprays: Types, Technology and Modeling Vella, M.C., Nova Science Publishers (ISBN: 978-161324345-9), 2011.

[77] H. Knozinger, P. Ratnasamy, Catal. Rev.-Sci. Eng., 17 (1978) 31-70.

[78] M. Digne, P. Sautet, P. Raybaud, P. Euzen, H. Toulhoat, J. Catal., 226 (2004) 54-68.

[79] C. Shi, M.J. Cheng, Z.P. Qu, X.H. Bao, Appl. Catal. B., 51 (2004) 171-181.

[80] S.J. Miao, Y. Wang, D. Ma, Q.J. Zhu, S.T. Zhou, L.L. Su, D.L. Tan, X.H. Bao, J. Phys. Chem. B., 108 (2004) 17866-17871.

[81] A. Musi, P. Massiani, D. Brouri, J.-M. Trichard, P. Da Costa, Catal. Lett., 128 (2009) 25-30.

[82] V.A. Kondratenko, U. Bentrup, M. Richter, T.W. Hansen, E.V. Kondratenko, Appl. Catal. B., 84 (2008) 497-504.

[83] K. Sato, T. Yoshinari, Y. Kintaichi, M. Haneda, H. Hamada, Appl. Catal., B. 44 (2003) 67-78.

[84] M. Mannikko, M. Skoglundh, H.H. Ingelsten, Appl. Catal., B. 119 (2012).

[85] A.N. Pestryakov, A.A. Davydov, J. Electron Spectrosc. Relat. Phenom. 74 (1995) 195-199.

[86] X. She, M. Flytzani-Stephanopoulos, J. Catal. 237 (2006).

[87] P. Sazama, L. Capek, H. Drobna, Z. Sobalik, J. Dedecek, K. Arve, B. Wichterlova, J. Catal., 232 (2005) 302-317.

[88] J. Lv, T. Kako, Z. Li, Z. Zou, J. Ye, J. Phys. Chem. C 114 (2010) 6157-6162.

[89] X. Yang, J. Xu, T. Wong, Q. Yang, C.-S. Lee, Phys. Chem. Chem. Phys. 15 (2013) 12688-12693.

[90] G. Zhu, L. Guo, X. Shen, Z. Ji, K. Chen, H. Zhou, Sens. Actuators B 220 (2015) 977-985.

[91] F. Zhang, X. Li, Q. Zhao, Q. Zhang, M. Tade, S. Liu, J. Colloid Interface Sci., 457 (2015) 18-26.

[92] J.Z. Yin, S.B. Huang, Z.C. Jian, M.L. Pan, Y.Q. Zhang, Z.B. Fei, X.R. Xu, Appl. Phys. A 120 (2015) 1529-1535.

[93] Q. Liu, W. Zhang, R. Liu, G. Mao, Eur. J. Inorg. Chem., (2015) 845-851.

[94] P.W. Park, C.S. Ragle, C.L. Boyer, M.L. Balmer, M. Engelhard, D. McCready, J. Catal., 210 (2002) 97-105.

[95] K.I. Hadjiivanov, Catal. Rev.-Sci. Eng., 42 (2000) 71-144.

[96] G.M. Underwood, T.M. Miller, V.H. Grassian, J. Phys. Chem. A., 103 (1999) 6184-6190.

[97] M.A. Centeno, I. Carrizosa, J.A. Odriozola, Appl. Catal. B., 19 (1998) 67-73.

[98] F. Acke, B. Westerberg, M. Skoglundh, J.Catal., 179 (1998) 528-536.

[99] M. Wallin, H. Gronbeck, A.L. Spetz, M. Skoglundh, Appl. Surf. Sci., 235 (2004) 487-500.

[100] C. Morterra, G. Magnacca, Catal. Today, 27 (1996) 497-532.

[101] R. Ferrando, J. Jellinek, R.L. Johnston, Chem. Rev., 108 (2008) 845-910.

[102] V. Celorrio, P.M. Quaino, E. Santos, J. Florez-Montano, J.J.L. Humphrey, O. Guillen-Villafuerte, D. Plana, M.J. Lazaro, E. Pastor, D.J. Fermin, ACS Catal., 7 (2017) 1673-1680.

[103] N.G. Semaltianos, R. Chassagnon, V. Moutarlier, V. Blondeau-Patissier, M. Assoul, G. Monteil, Nanotech., 28 (2017).

[104] A.N. Jiang, B.H. Zhang, Y.G. Xue, Y. Cheng, Z.H. Li, J.C. Hao, Microporous Mesoporous Mater., 248 (2017) 99-107.

[105] T. Szumelda, A. Drelinkiewicz, E. Lalik, R. Kosydar, D. Duraczynska, J. Gurgul, Appl. Catal. B., 221 (2018) 393-405.

[106] B. Sljukic, M. Martins, E. Kayhan, A. Balciunaite, T. Sener, C.A.C. Sequeira, D.M.F. Santos, J. Electroanal. Chem., 797 (2017) 23-30.

[107] Y.G. Sun, Y.D. Yin, B.T. Mayers, T. Herricks, Y.N. Xia, Chem. Mater., 14 (2002) 4736-4745.

[108] P. Jaroenapibal, P. Boonma, N. Saksilaporn, M. Horprathum, V. Amornkitbamrung, N. Triroj, Sens. Actuators B., 255 (2018) 1831-1840.

[109] A. Barrera, M. Viniegra, P. Bosch, V.H. Lara, S. Fuentes, Appl. Catal. B., 34 (2001) 97-111.

[110] H. Lorenz, S. Turner, O.I. Lebedev, G. Van Tendeloo, B. Klotzer, C. Rameshan, K. Pfaller, S. Penner, Appl. Catal. A., 374 (2010) 180-188.

[111] N. Basavegowda, K. Mishra, Y.R. Lee, New J. Chem., 39 (2015) 972-977.

[112] J.H. Cha, K.S. Kim, H. Lee, Korean J. Chem. Eng., 26 (2009) 760-764.

[113] Y. Hashimoto, G. Seniutinas, A. Balcytis, S. Juodkazis, Y. Nishijima, Sci. Rep., 6 (2016) 9.

[114] G.T. Fu, K. Wu, J. Lin, Y.W. Tang, Y. Chen, Y.M. Zhou, T.H. Lu, J.Phys. Chem. C., 117 (2013) 9826-9834.

[115] S. Hirasawa, H. Watanabe, T. Kizuka, Y. Nakagawa, K. Tomishige, J. Catal., 300 (2013) 205-216.

[116] Y. Somanoto, W.M. Sachtler, J. Catal., 32 (1974) 315-324.

[117] J.Y. Sun, Y.X. Han, H.Y. Fu, H.Q. Wan, Z.Y. Xu, S.R. Zheng, Appl. Surf. Sci., 428 (2018) 703-709.

[118] O. Terekhina, E. Roduner, J. Phys. Chem. C., 116 (2012) 6973-6979.

[119] O.S. Alexeev, S. Krishnamoorthy, C. Jensen, M.S. Ziebarth, G. Yaluris, T.G. Roberie, M.D. Amiridis, Catal. Today, 127 (2007) 189-198.

[120] M.S. Li, J.Y. Shen, Mater. Chem. Phys., 68 (2001) 204-209.

[121] D. Childers, A. Saha, N. Schweitzer, R.M. Rioux, J.T. Miller, R.J. Meyer, ACS Catal., 3 (2013) 2487-2496.

[122] J. Szanyi, J.H. Kwak, Phys. Chem. Chem. Phys., 16 (2014) 15126-15138.